

10

Conducting Multiphase Magnetic Nanocomposites for Microwave Shielding Application

Avanish Pratap Singh, Monika Mishra and S.K. Dhawan*

Materials Physics & Engineering Division, CSIR-National Physical Laboratory, New Delhi – 110012, India
*Corresponding author

Outline:

Introduction.....	247
Electromagnetic interference shielding and microwave absorption	248
<i>Shielding effectiveness</i>	249
<i>Absorption loss</i>	250
<i>Reflection loss</i>	251
<i>Multiple reflections</i>	251
<i>Measurement Methods of microwave properties</i>	251
<i>Measurement of Shielding Effectiveness</i>	251
<i>Measurement of complex permeability and permittivity</i>	251
<i>Conduction in microwave field</i>	252
<i>Orientation polarization</i>	253
<i>Interfacial or space charge polarization</i>	253
Materials and fillers for microwave shielding	253
Synthesis of Multiphase Nanocomposites	256
Synthesis of Multiphase Nanocomposites-1 (Synthesis of polyaniline composite having conducting (rGO) and magnetic (γ -Fe ₂ O ₃) phase)	256
<i>Characterization</i>	257
<i>Surface morphology and microstructural studies of composite</i>	257
<i>Structural Analysis</i>	258
<i>Raman Spectroscopy</i>	259
<i>Conductivity, magnetic & dielectric properties of the composites</i>	260
<i>Electromagnetic shielding</i>	263
Synthesis of Multiphase Nanocomposites-2 (Synthesis of hybrid composite having γ -Fe ₂ O ₃ nanoparticles, fly ash, and conducting matrix)	266
<i>Characterization</i>	268
<i>Surface morphology and microstructural studies of composite</i>	268
<i>Structural Analysis</i>	269
Conclusions.....	272
References.....	272

Introduction

With the rapid development of electronic technology, mobile communication and satellite communication, electromagnetic interference (EMI) has become one of the main factor to weaken electronic system performance and thus, electromagnetic interference is considered as modern environment pollution[1, 2]. Due to increasing government regulations to control the level of electromagnetic radiations in the environment due to health hazard, and also the new norms and issues regarding the compatibility and EMI, many efforts have been made to reduce its effects using microwave shielding materials[3]. Electromagnetic materials have dielectric and/or magnetic losses, and dependence of these losses on frequency is responsible for their performance, resulting in absorption and/or scattering of electromagnetic waves. Traditionally, metals particularly in the form of thin sheets were used against electromagnetic shielding[4]. However, expensiveness, heaviness, prone to corrosion and difficult to process are few drawbacks when metal is used as a shielding material. Thus, graphene, multiwalled carbon nanotubes (MWCNT), expanded graphite and conducting polymers like polyaniline, polypyrrole and PEDOT embedded with nano ferrite materials like γ -Fe₂O₃, barium ferrite (BaFe₁₂O₁₉) and suitable dielectric matrix like barium titanate, barium strontium titanate, TiO₂, flyash, silica etc. are designed which can be alternative material for microwave shielding because of light weight, cheap, resistant to corrosion and easily processable[5-11]. Therefore, a wide variety of materials in the recent past have been used for EMI shielding with broad range of electrical conductivity, good electromagnetic attributes such as permittivity, permeability and engineered geometries[12-14]. The capability to shield electromagnetic waves depends on materials electrical conductivity permittivity and permeability. Three types of electromagnetic shielding mechanism have been proposed, namely: reflection, absorption and multiple reflections. The primary mechanism of shielding is the reflection loss (SE_R) which is the result of the interaction between the conducting particles in the conducting material (free electron or vacancy) and the EM field[8]. While the absorption loss depends on the value of σ_r/μ_r , i.e., the absorption loss is maximum when $\mu_r = \sigma_r$. Thus, the shielding mechanism of multiphase nanocomposites will be studied by quantifying the contribution of absorption and reflection loss to the total EMI shielding effectiveness (SE) along with the correlation among the conductivity, $\tan \delta$, absorption loss, reflection loss, magnetic properties and composite morphology[15, 16]. The developing role of graphene, conducting polymers, ferrites nanocomposites as microwave shield is discussed in this chapter. Graphene-based composites, derived from the decoration of graphene nanosheets with different nanoparticles (NPs), have emerged as a class of intriguing materials from both perspectives of science and technology[17-19]. The multifunctional composites can combine the advantages of both graphene and NPs. More attractively, these functionalized nanocomposites exhibit new or enhanced properties which warrant them as promising materials with applications in wide areas. Therefore a series of efforts using partially reduced graphene oxide with different matrix has been investigated for microwave shielding in which graphene oxide–ferrofluid–cement nanocomposite has significant interest i. e. incorporation of graphene oxide (30 wt%) along with an appropriate amount of ferrofluid in the cement matrix leads to a shielding effectiveness of 46 dB (>99% attenuation) towards composite[20].

In this chapter, EMI shielding performance of polymer based multiphase composite and graphene based multiphase composite are broadly investigated. In the first investigation, to enhance the properties of conducting polymer for developing EMI shielding material, an effort has been made in which γ -Fe₂O₃ decorated rGO filled in polyaniline (PANI) tube core-shell structure has been synthesized for microwave absorption. The selectivity of the different materials to synthesize present composites

are based on the associated properties of these compounds to fabricate the desired material with all required property for EMI shielding in a single composite. The core-shell tubular structure associated with RF particles embedded in polymer chains attributes the enhanced interfacial polarization and the effective anisotropy energy of composite, as a result more and more scattering occurs which leads to the high SE ($SE_T \sim 51\text{dB}$) in comparison to conventional materials. The synthesized in-filled novel micro tubes have better microwave absorption properties ($SE_A \sim 43\text{dB}$) which strongly depends upon optimal infilling of RF in PANI matrix. Additionally, the microwave absorption properties can be tailored easily by varying the PANI/RF ratio and thickness of the samples. In the second investigation, expanded graphite (EG) was incorporated into fly ash matrix along with nanoferrite $\gamma\text{-Fe}_2\text{O}_3$ particles so that the resultant conductive fly ash composite can be used for electromagnetic shielding in microwave range. Conductivity of composites lies in the range 0.34–32.86 S/cm. TEM images show that fly ash particle (0.87 μm) is covered by sheets of EG containing the magnetic nano particles. Complex parameters have been calculated from experimental scattering parameters (S_{11} & S_{21}) using theoretical calculations given in Nicholson–Ross and Weir algorithms. The microwave absorption properties of the composites have been studied in the 8.2–12.4GHz (X–Band) frequency range which shows a shielding effectiveness up to 90 dB, which strongly depends on dielectric loss and weight fraction of fly ash and $\gamma\text{-Fe}_2\text{O}_3$ in EG matrix.

In addition, this chapter also establishes current trends and challenges in shielding research and opens arena for the development of futuristic radar absorbing materials.

Electromagnetic interference shielding and microwave absorption

EMI shield is essentially a barrier to block undesired electromagnetic (EM) induction triggered by alternating current/voltage which tries to produce corresponding induced signals (voltage and current) in the nearby electronic circuitry, thereby trying to spoil its performance[21]. In power electronics, the term shielding usually refers to an enclosure that completely encloses an electronic product or the portion of that product and prevents the EM emission from an outside source to deteriorate its electronic performance. Conversely, it may also be used to prevent an external susceptible (electronic items or living organisms) from internal emissions of an instrument's electronic circuitry. Shielding is the process by which a certain level of attenuation is extended using a strategically designed EM shield. The shielding efficiency is generally measured in terms of reduction in magnitude of incident power/field upon transition across the shield. Shielding is required for proper functioning and unperturbed operation of electronics by preventing the radiated emission outside the product from coupling to the product electronics that may cause interference in the product or to prevent the product from causing interference with the other electronic products. And it can be performed in two ways as illustrated in Figure 10.1. First, prevent the radiated electromagnetic signals emitted by electrical circuits under operation (Figure 10.1a) second; avoid the radiation outside the boundaries of the product (Figure 10.1b). Therefore, conceptually, shield act as a barrier to the transmission of the electromagnetic field. Furthermore, shielding effectiveness is defined as the ratio between the field strength at a given distance from the source without the shield imposed and the field strength with the shield imposed.

If electronic item is placed inside a thin, conductive shell that is placed in an E-field, it will be shielded because the current setup by the electromagnetic wave does not conduct inside of the shell. This is not because the shell has completely absorbed the field but because the E-field has caused electronic charges of different polarity along the shell. These charges generate an electrical field that will tend to

cancel the original field inside the shell[22, 23]. When it comes to H-fields, shields made of a soft magnetic material with high permeability, $\mu \gg 1$, and sufficient thickness attenuate the magnetic field in the shielding shell by providing a low reluctance. That is, the spherical shell of magnetic material with good permeability will reduce the H-field intensity inside because the H-field tends to remain in the magnetic material layer as the magnetic material offers a low-reluctance path[22, 24].

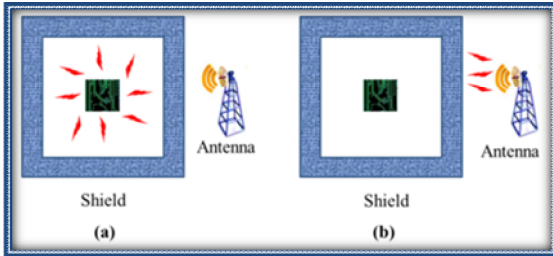


FIGURE 10.1

Illustration of the use of a shielded enclosure **(a)** radiation from an electrical circuit under operation **(b)** to exclude radiation from the outside radiation source[25]

Alternatively, a thin shield made of a conductive material with low permeability can also provide effective shielding for H-fields at high frequencies. This is because an alternating H-field will induce eddy currents in the shielding screen, assuming that the shield has adequate conductivity. These eddy currents will themselves create an alternating H-field of the opposite orientation inside the shell. The effect will increase as the frequency increases, resulting in high shielding effectiveness at high frequencies.

Shielding effectiveness

The shielding effectiveness of a shield depends on EMI attenuation, frequency, the distance of the shield from the source, the thickness of the shield and the shield material. Shielding effectiveness (SE) is normally expressed in decibels (dB) as a function of the logarithm of the ratio of the incident and exit electric (E), magnetic (H), or plane-wave field intensities (P)

$$SE(dB) = 10 \log\{P_T / P_I\} = 20 \log\{E_T / E_I\} = 20 \log\{H_T / H_I\} \tag{1.1}$$

where P_I (E_I or H_I) and P_T (E_T or H_T) are the power (electric or magnetic field) of incident and transmitted EM waves respectively. With any kind of electromagnetic interference, there are three mechanisms contributing to the effectiveness of a shield. Part of the incident radiation is reflected from the front surface of the shield, part is absorbed within the shield material and part is reflected from the shield rear surface to the front where it can aid or hinder the effectiveness of the shield depending on its phase relationship with the incident wave, as shown in eqn. 1.2.

Therefore, the total shielding effectiveness of a shielding material (SE) equals the sum of the absorption factor (SE_A), the reflection factor (SE_R) and the correction factor to account for multiple reflections (SE_M) in thin shields given by[26-30]

$$SE(dB) = SE_A + SE_R + SE_M \tag{1.2}$$

According to Schelkunoff's theory, SE_M can be ignored in all practical application where the shield is thicker than the skin depth (δ). For a material, the skin depth (δ) is the distance up to which the intensity of the EM wave decreases to $1/e$ of its original strength.

Absorption loss

Absorption loss SE_A , is a function of the physical characteristics of the shield and is independent of the type of source field. Therefore, the absorption term SE_A is the same for all the three waves. When an electromagnetic wave passes through a medium, its amplitude decreases exponentially (Figure 10.2). This decay or absorption loss occurs because currents induced in the medium produce ohmic losses and heating of the material, where E_1 and H_1 can be expressed as $E_1 = E_0e^{-t/\delta}$ and $H_1 = H_0e^{-t/\delta}$ [27]. The distance required by the wave to be attenuated to $1/e$ or 37% is defined as the skin depth[16, 31]. Therefore, the absorption term SE_A in decibel is given by the expression:

$$SE_A(dB) = 20 \frac{t}{\delta} \log e = 8.68 \frac{t}{\delta} \tag{1.3}$$

where, t is the thickness of the shield in mm; f is frequency in MHz; μ is relative permeability (1 for copper); σ is conductivity relative to copper. The skin depth δ can be expressed as:

$$\delta = \sqrt{2 / \sigma \omega \mu'} \tag{1.4}$$

The absorption loss of one skin depth in a shield is approximately 9 dB. Skin effect is especially important at low frequencies where the fields experienced are more likely to be predominantly magnetic with lower wave impedance than 377Ω . From the absorption loss point of view, a good material for a shield will have high conductivity and high permeability along with a sufficient thickness to achieve the required number of skin depths at the lowest frequency of concern.

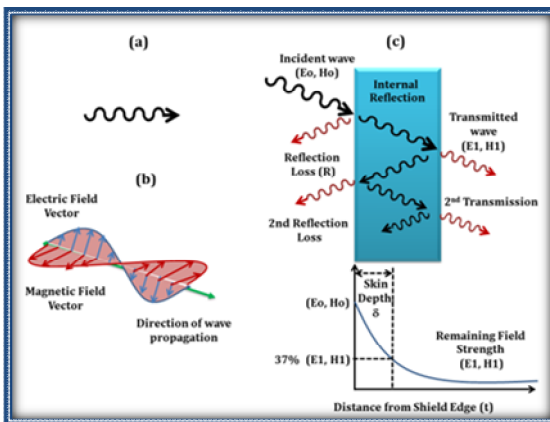


FIGURE 10.2

Graphical illustration of EMI shielding mechanism, (a) EM wave representation, (b) shows the electric and magnetic field vector are perpendicular to the direction of wave propagation (c) Splitting of electromagnetic wave on passing through a shield[21, 32]

Reflection loss

The reflection loss is related to the relative mismatch between the incident wave and the surface impedance of the shield. The computation of reflection losses can be greatly simplified by considering shielding effectiveness for incident electric fields as a separate problem from that of electric, magnetic or plane waves. The equations for the three principle fields are given by the expressions[27]

$$R_E = K_1 10 \log \left(\frac{\sigma}{f^3 r^2 \mu} \right) \quad (1.5)$$

$$R_H = K_2 10 \log \left(\frac{f r^2 \sigma}{\mu} \right) \quad (1.6)$$

$$R_p = K_3 10 \log \left(\frac{f \mu}{\sigma} \right) \quad (1.7)$$

where, R_E , R_H , and R_p are the reflection losses for the electric, magnetic and plane wave fields, respectively, expressed in dB; σ is the relative conductivity relative to copper; f is the frequency in Hz; μ is the relative permeability relative to free space; r is the distance from the source to the shielding in meter.

Multiple reflections

The factor SE_M can be mathematically positive or negative (in practice, it is always negative) and becomes insignificant when the absorption loss $SE_A > 6$ dB. It is usually only important when metals are thin and at low frequencies (i.e., below approximately 20 kHz). The formulation of factor SE_M can be expressed as

$$SE_M = -20 \log(1 - e^{-2t/\delta}) \quad (1.8)$$

Measurement Methods of microwave properties

Measurement of Shielding Effectiveness

EMI SE is generally measured under far field conditions using Vector Network Analyser which consists of a spectrum analyser and a specifically designed coaxial line to give 50 Ω impedance. There are two advantages of coaxial transmission line measurement, first the measurement is independent of the investigator, and second, the ration of reflection and transmission in a 50 Ω line are the same as would be obtained in free space[7].

Measurement of complex permeability and permittivity

Presently the most widely technique used for driving complex permittivity and permeability is the transmission line loaded either with waveguides or coaxial line. In the techniques, the incident EM wave refracted with the sample and induces a reflected wave (S_{11}) and transmitted wave (S_{21}). The

Weir[13] and Nicolson[33] proposed a method for calculating complex permittivity and permeability using these scattering parameters, in the 50 MHz to 18 GHz frequency range. Reflection and transmission coefficients (S parameters) are recorded by inserting the test sample in a sample holder connected between the waveguide flanges of network analyzer as shown in Figure 10.3. In order to avoid significant measurement errors, test sample must be prepared such that it must be tightly fit in the cross section of sample holder. In the rectangular waveguide measurements, the different size sample used for different frequency range e.g. $22.8 \times 10 \text{ mm}^2$ for X (8.2-12.4 GHz) band and $15.8 \times 7.9 \text{ mm}^2$ for P (12.4-18 GHz) band frequency range.

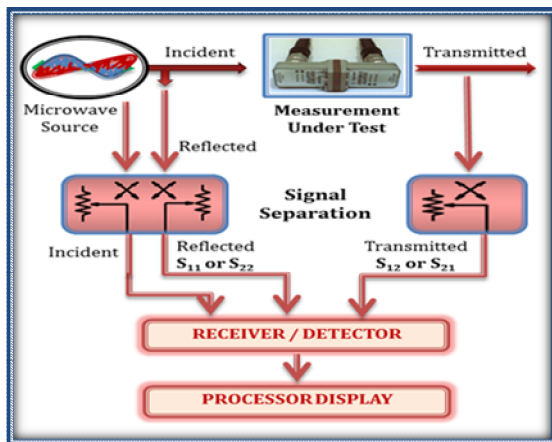


FIGURE 10.3

General principal of a spectrum analyzer for driving the dielectric attributes of materials[34-36]

Conduction in microwave field

At the microscopic level, a material may have several dielectric mechanisms or polarization effects that contribute to its overall permittivity (Figure 10.4). When an electric field is applied to a material, an induced dipole moment connected to the polarisability appears. This dipole moment comes from nonhomogeneous repartition of charges which results in several types of polarization[7]

- The electronic cloud displacement around the atom called electronic polarization.
- Applied electric field can modify the electron repartition and consequently the equilibrium location of the atoms in the molecule, known as the atomic polarization.
- Even after switching off the electric field, permanent dipole moment exist that causes dipolar polarization.

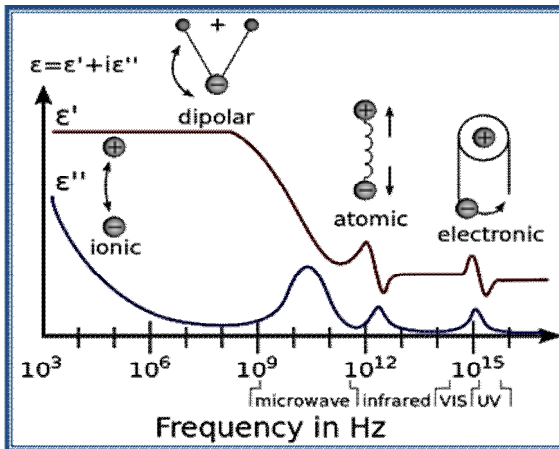


FIGURE 10.4
Dielectric mechanism [34, 37]

Orientation polarization

Permanent dipole moments are oriented in a random manner in the absence of an electric field so that no polarization exists. The electric field 'E' will exercise torque 'T' on the electric dipole, and the dipole will rotate to align with the electric field causing orientation polarization to occur. The friction accompanying the orientation of the dipole will contribute to the dielectric losses. The dipole rotation causes a variation in both ϵ' and ϵ'' at the relaxation frequency which usually occurs in the microwave region.

Electronic and atomic polarization

Electronic polarization occurs in neutral atoms when an electric field displaces the nucleus with respect to the electrons that surround it. Atomic polarization occurs when adjacent positive and negative ions "stretch" under an applied electric field. The amplitude of the oscillations will be small for any frequency other than the resonant frequency.

Interfacial or space charge polarization

Interfacial or space charge polarization occurs when the motion of migrating charges is impeded. The charges can become trapped within the interfaces of a material. Motion may also be impeded when charges cannot be freely discharged or replaced at the electrodes. The field distortion caused by the accumulation of these charges increases the overall capacitance of a material which appears as an increase in ϵ' .

Materials and fillers for microwave shielding

The basic theory of SE as discussed in section 2, revealed that an ideal microwave shield must be a multiphase composite which contain the optimum concentration of electrically conducting material,

dielectric filler and magnetic material. Along with this, physical geometry also plays crucial role in improving the SE. Moderate conductivity (10^{-4} to 10^{-1} S/cm) of the composite improves SE in two ways, first, incident EM wave reflected from the front face of conducting shield because interaction of electric vector with mobile charge carriers present on conducting surface resulted in ohmic losses (heat). Second, for materials consisting of a high concentration of charge carriers (i.e., with a high conductivity), polarization due to the migration of charge carriers to form space charges at interfaces or grain boundaries becomes important. This space charge polarization enhances the polarization effect [15, 38].

Presence of dielectric filler in multiphase composite increases the dielectric constant of the shield which further accompanied with high-dielectric losses. To raise the dielectric constant of multiphase composites, high-dielectric constant ceramic powders such as TiO_2 , SiO_2 , ZnO , fly ash, barium titanate, strontium titanate, barium strontium titanate and PbTiO_3 have been added[39-41]. High permeability materials are purposely added in multiphase composite to increase the magnetic losses which is the combined result of eddy current effects, natural resonances and anisotropy energy present in the composites[20]. In the microwave ranges, the presence of nano ferrite particles in the composite is the main cause of eddy current.[21] Therefore, around the globe, various research groups tried to design an effective shield against electromagnetic radiation using a combination of filler having conducting part (e.g. conducting polymers[42, 43], graphitic materials[35], CNTs[44, 45] and carbon fiber[46]), magnetic part (iron nickel[47], soft[20] and hard ferrites[16]) and insulating or dielectric part (e.g. BaTiO_3 , TiO_2 , Flyash)[40, 48].

In this series, Lei wang et.al prepared graphene@ Fe_3O_4 @ SiO_2 @NiO nanosheets combining sol-gel process and hydrothermal reaction. The microwave absorption properties of graphene@ Fe_3O_4 and graphene@ Fe_3O_4 @NiO nanosheets were investigated between 2-18 GHz. The maximum reflection loss of graphene@ Fe_3O_4 @NiO nanosheets was -51.5 dB at 14.6 GHz with a thickness of 1.8 mm[49]. Another example of multiphase composite is given by Ren et.al. who has built a microwave absorbing shield using graphene/ Fe_3O_4 @Fe/ZnO quaternary nanocomposites. Results showed that the maximum absorption for the quaternary nanocomposites was less than -30 dB with the thickness 2.5-5 mm (in the frequency range of 5.9-15.2 GHz)[50]. Yang et.al synthesized bowl-like Fe_3O_4 hollow spheres/reduced graphene oxide nanocomposites, as synthesized nanocomposites with a coating layer thickness of 2 mm exhibited a maximum absorption loss of -24 dB at 12.9 GHz as well as a bandwidth of 4.9 GHz (from frequency of 10.8-15.7 GHz) corresponding to reflection loss at -10 dB[51]. Qin Li et.al prepared magnetic composites of barium ferrite coated flyash cenospheres by sol-gel auto-combustion method. The barium ferrite coated flyash powder-epoxy composites possesses excellent microwave absorption properties in the 2-18 GHz frequency range with the maximum reflection loss -15.4 dB at 8.4 GHz with a sample thickness of 2.0 mm[52]. W.L. Song et.al fabricated flexible graphene/polymer composite films into paraffin-based sandwich structures to evaluate electromagnetic interference (EMI) shielding. They optimized shielding effectiveness up to 27 dB suggested effective shielding of the composites films[53]. Same group synthesized carbon nanosheet/wax composites showing maximum reflection loss up to 60 dB.[54] Seo et.al have evaluated the EMI shielding of the single walled carbon nanotubes coated PET synthesized by the spin coating technique with enhanced EMI shielding in the terahertz region[55]. Zhang et.al prepared poly(methyl methacrylate)-based bulk foams embedded with chemically reduced graphene oxide by blending and then foamed by environmentally benign subcritical CO_2 foaming technique with excellent EMI shielding up to 19 dB[6]. Xu Huang et.al successfully synthesized BaTiO_3 @MWCNTs core/shell hetrostructure via solvent-thermal method. The maximum peak value of BaTiO_3 @MWCNTs hetrostructure (10:1) reaches -45 dB at 5.5 GHz when the thickness of absorber layer is 3.5 mm.[41] Yang et.al demonstrated a small quantity of carbon nanotubes dispersed into the void space between carbon nanofibers within a polymer matrix and the

influence of this combination on the EMI shielding was investigated. The shielding effectiveness increased dramatically up to 20.3 dB which is required for commercial applications. [46] Yang et.al also synthesized a novel carbon nanotube-polystyrene foam composite for EMI shielding applications. The EMI shielding provided by the composite was around 20 dB for 7 wt % CNT loading[56]. Chen Sun et.al were successfully synthesized FeNi/RGO nanocomposites through in-situ reduction. Sphere-like FeNi nanoparticles were deposited on the RGO nanosheets. The FeNi/RGO nanocomposites show outstanding EM absorption properties in the 2-18 GHz range, as evidenced by the wide effective absorption bandwidth (up to 3.3 GHz, with reflection loss RL less than 10 dB).[57] Das et.al has been successfully prepared the composites based on DBSA-doped polyaniline and $\text{BaTiO}_3/\text{Ni}_{0.5}\text{Zn}_{0.5}\text{Fe}_2\text{O}_4$ in epoxy resin matrices. It has shown maximum reflection loss of -15.78 dB at 10.89 GHz. For these composites, magnetic losses were less important and dielectric loss and the joule-heating loss has major contribution to the loss mechanism[38]. Brigandi et.al shown the use of multiphase polymer blends provide unique morphologies and properties to reduce the percolation concentration and increase conductivity of carbon based polymer composites. It is clear that the development of new CPC represent significant opportunity for material solutions to improve performance in application such as electromagnetic interference shielding.[58] Li et.al fabricated single-walled carbon nanotube-epoxy composites using in situ process. The highest EMI shielding was obtained for 15 wt % SWCNT, up to 49 dB at 10 MHz and exhibiting 15-20 dB in the 500 MHz to 1.5 GHz range[59]. Kim et.al studied the electrical conductivity and EMI shielding properties of multi-walled carbon nanotube-PMMA composite containing Fe. They report 27 dB for 40 % MWCNTs loading[60]. Xiang et.al synthesized MWCNT/silica composites and shown their microwave shielding properties in the 8.2 to 12.4 GHz range[61]. Che et.al prepared Fe encapsulated carbon nanotube composite by CVD technique and composites were studied for microwave shielding properties. The maximum reflection loss was 25 dB for the composite in the frequency range 2-18 GHz[9]. Wang et.al reported ternary dense bulk composites of ordered mesoporous carbon/ordered mesoporous silica/fused silica prepared by in-situ nanocasting in combination with hot-pressing. They show maximum total EMI shielding up to 28.2 dB[62].

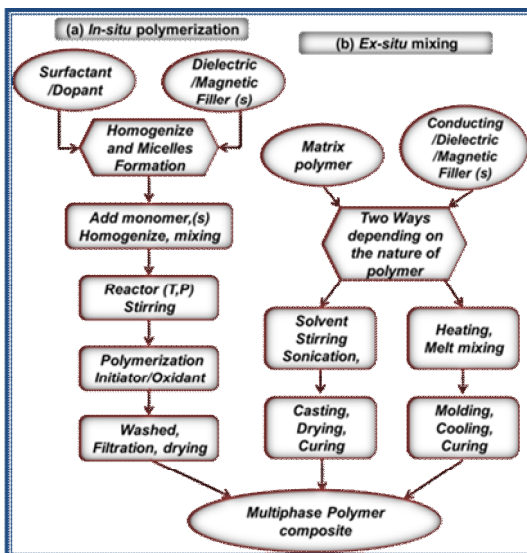


FIGURE 10.5

(a) Flow chart for the synthesis of polymer composites by *in-situ* polymerization route and (b) flow chart showing the steps involved in the formation of multiphase composite *ex-situ* mixing

Synthesis of Multiphase Nanocomposites

On the basis of synthesis and fabrication of multiphase composites in last few decades, we can divide them in two categories, polymer based nanocomposites and composites having balanced weight ratio of conducting, magnetic and dielectric filler.[7, 21] Figure 10.5 a & b shows that polymer based composites may be designed by *in-situ* polymerization or *ex-situ* mixing, by solution processing and by melting/mixing/blending. Among these options *in-situ* polymerization has the advantages of design flexibly, filler incorporation ability and tailoring properties like conductivity, magnetization and dielectric attributes of the material which depend on dopant selection, filler and polymerization conditions like temperature, pressure, agitation conditions. On the other hand *ex-situ* mixing leads to poor dispersion of filler, agglomeration of filler particles and non-repeatability of results. Multiphase composites using *ex-situ* mixing are formed either by solution processing or by heating/melt mixing. In solution processing method, polymers are dissolved in a proper solvent by sonication or stirring to achieve homogeneous mixing followed by casting and curing, while, melt mixing involves the heating of polymer with filler followed by molding and cooling/curing.

Synthesis of Multiphase Nanocomposites-1

(Synthesis of polyaniline composite having conducting (rGO) and magnetic ($\gamma\text{-Fe}_2\text{O}_3$) phase)

The in-situ emulsion polymerization of aniline was carried out in the presence of $\gamma\text{-Fe}_2\text{O}_3$ decorated rGO (RF) particles to prepare PRF composites. Prior to PRF synthesis, In-situ synthesis of $\gamma\text{-Fe}_2\text{O}_3$ nanoparticles on the rGO matrix were carried out by taking 1:1 wt. ratio of rGO and $\text{Fe}(\text{acac})_3$ and the resultant composite were abbreviated as RF. The synthesis of RF and rGO were discussed in detail in our earlier report.[31] $\beta\text{-NSA}$ was used as a dopant without an external template. This method belongs to the self-assembly process^{39,40} because $\beta\text{-NSA}$ works as a dopant and a template functioning at the same time. A typical preparation process for PANI-RF composite is as follows: 0.3 M solution of $\beta\text{-NSA}$ and calculated amount of RF was homogenized (ART MICCRA D8 rotating at 17600 rpm for 2-h,) to obtain a uniform suspension containing RF particles. 0.1 M aniline has been added and stirring continued for another 1h to form an emulsion. Due to amphiphilic and surfactant nature, $\beta\text{-NSA}$ molecule (with hydrophilic SO_3H head and hydrophobic tail) easily forms micelles in aqueous solution. The aniline- $\beta\text{-NSA}$ mixture containing RF particles were cooled in an ice bath for 2-h before oxidative polymerization. Finally, the oxidant APS (0.1 M) was added drop wise to the above solution keeping the temperature of the reactor at 0°C with vigorous stirring for 10-h. The green polymer precipitates so obtained were treated with methanol in order to remove oligomers. The resulting precipitate was filtered and washed thoroughly till the filtrate became colorless and then dried at $60\text{--}65^\circ\text{C}$ in a vacuum oven for 24-h. Throughout the experiment, the molar ratio of aniline to $\beta\text{-NSA}$ and APS was retained at 1:3 and 1.0, respectively. However, the concentration of RF particles was changed to understand the effect of RF particles on the morphology, structure, electrical properties and shielding effectiveness of the resulting PANI-PRF composite tubes. Such a cooperative combination of $\beta\text{-NSA}$ (a non-corrosive organic dopant having surfactant traits), RF nanoparticles (conducting, magnetic and dielectric filler or guest) and PANI (electrically conducting matrix or host), can offer advantages such as good electrical, magnetic and dielectric properties which may collectively contribute towards high microwave absorption efficiency. Several compositions having different AN:RF weight ratios, i.e., 1:0, 1:1, 1:2 and 1:3, were prepared and designated as PRF10, PRF11, PRF12 and PRF13, respectively. Schematic

representation of incorporation of RF into PANI matrix is given in Figure 10.6. This scheme which suggests that rGO and $\gamma\text{-Fe}_2\text{O}_3$ embedded in PANI tubes leads to the formation of PANI composites which has better electrical and magnetic properties. The presence of rGO containing iron oxide nano particles in polymer matrix has been confirmed by the XRD of the composites. The presence of $\gamma\text{-Fe}_2\text{O}_3$ magnetic nanoparticles in RGO matrix has been confirmed by TEM.

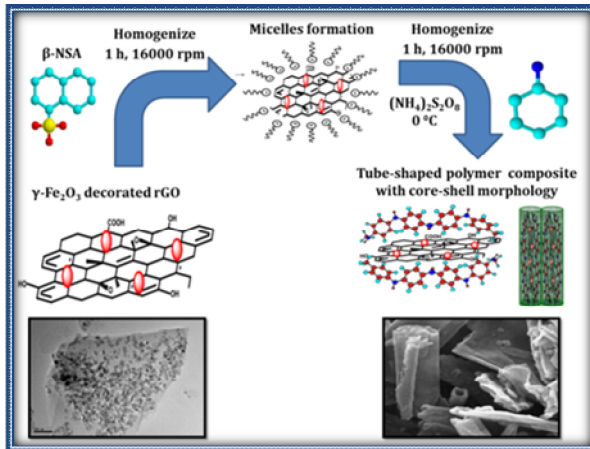


FIGURE 10.6

Schematic representation of fabrication of $\gamma\text{-Fe}_2\text{O}_3$ nanoparticles decorated rGO sheets filled in PANI tubes by *in-situ* polymerization of aniline using APS as oxidant in the presence of $\beta\text{-NSA}$. Reprinted with permission from ref. 15. Copyright 2014, Royal Society of Chemistry

Characterization

Surface morphology and microstructural studies of composite

SEM has been carried out to determine the distribution of rGO or rGO platlets and $\gamma\text{-Fe}_2\text{O}_3$ in the polymer matrix. Figure 10.7 (a) shows the agglomerated magnetic nanoparticles derived from thermal decomposition of $\text{Fe}(\text{acac})_3$. The estimated particle size of rGO has been found up to few micrometer as shown in Figure 10.7 (b). Although, thickness of rGO sheets and particle size of $\gamma\text{-Fe}_2\text{O}_3$ have not been possible to explore via SEM technique. The inset show the distribution of nanoparticles of $\gamma\text{-Fe}_2\text{O}_3$ on the surface of rGO sheet. SEM image of PANI composites synthesized in the presence of $\beta\text{-NSA}$ reveal an interesting morphology featuring formation of tube like structure (Figure 10.7 (c)). Densely packed tubes have a range of diameter and length of ~ 0.5 to $2\mu\text{m}$ and up to $15\mu\text{m}$, respectively. SEM micrograph of PANI composites reveals that RF particles are entrapped within the PANI matrix (Figure 10.7 (d)). This reduces the length of the tubes and increases the roughness of the surface. The diameter of PANI composite is larger than the pristine PANI.

Figure 10.8 demonstrates the TEM/HRTEM images of $\gamma\text{-Fe}_2\text{O}_3$, rGO sheet, RF, pristine PANI and PANI composites. Figure 10.8 (a) shows the iron oxide nanoparticles derived from $\text{Fe}(\text{acac})_3$ by thermal decomposition at $186\text{ }^\circ\text{C}$ in an organic solvent. The lattice plane spacing of the $\gamma\text{-Fe}_2\text{O}_3$ particles is about 0.29 nm which corresponds to the 206 plane as shown in Figure 10.8 (b). It was first confirmed with the XRD pattern of the $\gamma\text{-Fe}_2\text{O}_3$ phase. Figure 10.8 (c) shows the HRTEM image of a few rippled rGO nanosheets which clearly indicates the graphitic lattice. The interplanar distance has been measured to be 0.37 nm , corresponding to the spacing of the 002 planes. This is consistent with the

result calculated from XRD analysis, Figure 10.9 (a). The dispersion of γ -Fe₂O₃ in rGO matrix is confirmed by the HRTEM image (Figure 10.8 (d)). Figure 10.8 (e) shows the PANI tubes having diameter $\sim 1.75 \mu\text{m}$ and length $\sim 6 \mu\text{m}$. PANI tubes are filled with a mixture of nanoferrite particles and rGO. Diameter of PANI composite is more in comparison of the pristine PANI tubes (Figure 10.8 (f)). The presence of rGO (conducting filler) and γ -Fe₂O₃ nanoparticles (magnetic filler) in the core of PANI is helpful for improving matching of ϵ_r and μ_r which is necessary for enhancing the absorption of the EM wave.

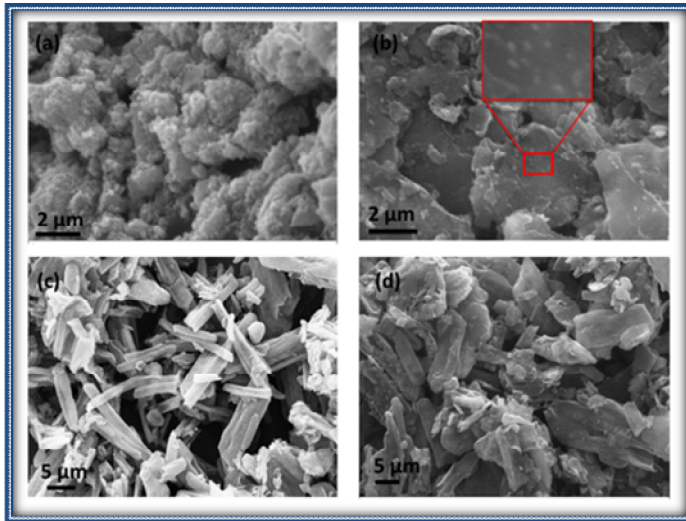


FIGURE 10.7

SEM images of (a) iron oxide nanoparticles derived from Fe(acac)₃ by thermal decomposition at 186 °C, (b) reduced graphene oxide sheets decorated with γ -Fe₂O₃ nanoparticles, (c) PRF10 and (d) PRF13, showing the formation of tube like structure with RF particles inside the tubes. Reprinted with permission from ref. 15. Copyright 2014, Royal Society of Chemistry

Structural Analysis

Figure 10.9 (a) shows the XRD patterns of γ -Fe₂O₃, RF, pristine PANI, and PANI composite. The main peaks for γ -Fe₂O₃ are observed at $2\theta=30.265^\circ$ ($d=2.9530 \text{ \AA}$), $2\theta=35.659^\circ$ ($d=2.5177 \text{ \AA}$), $2\theta=43.320^\circ$ ($d=2.0886 \text{ \AA}$), $2\theta=57.321^\circ$ ($d=1.6073 \text{ \AA}$) and $2\theta=62.981^\circ$ ($d=1.4758 \text{ \AA}$) corresponding to the (2 2 0), (3 1 1), (4 0 0), (5 1 1) and (4 4 0) reflections, respectively. All observed peaks of γ -Fe₂O₃ have been matched with the standard XRD pattern (Powder Diffraction File, JCPDS No. 39–1346). The peaks present in γ -Fe₂O₃ have also been observed in iron incorporated rGO composite sheets which indicate the presence of ferrite particles in the rGO matrix. The presence of rGO is confirmed by the broad peaks at $2\theta=26.441^\circ$ ($d=3.368$), $2\theta=54.599^\circ$ ($d=1.679 \text{ \AA}$). PANI shows two broad peaks at $2\theta=19.795^\circ$ ($d=4.481 \text{ \AA}$) and 25.154° ($d=3.537 \text{ \AA}$), which reveals its amorphous nature.[63] The peaks of RF observed in PRF13 confirm the presence of a RF hybrid in the polymer matrix. The crystallite size of γ -Fe₂O₃ particle can be calculated by using Debye Scherrer's formula, $D=k\lambda/\beta\cos\theta$, where, D is crystalline size, λ is the X-ray wavelength, K the shape factor, θ is the half angle in degrees, and β is the line broadening measured by half-height in radians. The value of k is often assigned a value of 0.89, which depends on several factors, including the Miller index of the reflecting plane and the shape of the crystal. The average size of γ -Fe₂O₃ particles has been calculated using the above equation and estimated as 8.99

nm for pure $\gamma\text{-Fe}_2\text{O}_3$ and 9.83 nm for iron incorporated rGO. The peaks at $2\theta=30.265^\circ$ ($d=2.9530 \text{ \AA}$), $2\theta=35.659^\circ$ ($d=2.5177 \text{ \AA}$) for $\gamma\text{-Fe}_2\text{O}_3$ in the PANI composites show the formation of composites having separate phases of both compounds properly dispersed in the polymer matrix.

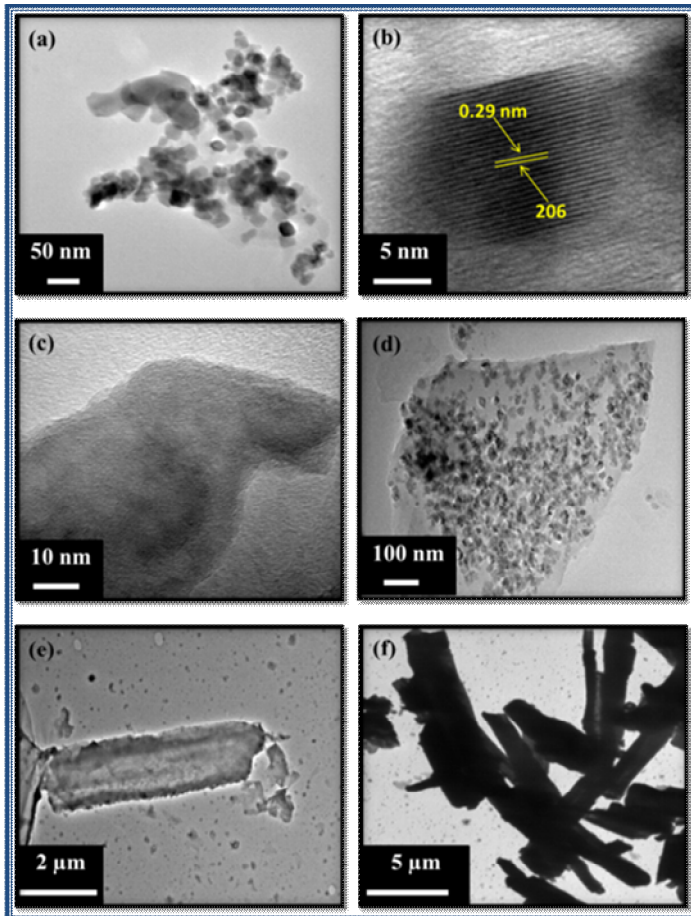


FIGURE 10.8

(a) TEM image of $\gamma\text{-Fe}_2\text{O}_3$, (b) High magnification HRTEM image of $\gamma\text{-Fe}_2\text{O}_3$ showing the 206 oriented lattice planes of $\gamma\text{-Fe}_2\text{O}_3$, (c) TEM image of rGO sheets, (d) TEM image of rGO- $\gamma\text{-Fe}_2\text{O}_3$ hybrid structure, showing the nanoparticles of $\gamma\text{-Fe}_2\text{O}_3$ on the rGO surface, (e) TEM micrographs of pristine PANI tube and (f) PANI tubes filled with a mixture of rGO- $\gamma\text{-Fe}_2\text{O}_3$. Reprinted with permission from ref. 15. Copyright 2014, Royal Society of Chemistry

Raman Spectroscopy

Raman spectroscopy is an important tool to identify the proper interaction or bonding between two components[64]. Figure 10.9 (b) shows the Raman spectra of RGO, RF, PRF10, and PRF13. The Raman spectra of RGO consist of three prominent characteristic peaks, namely the D band, the G band, and the G' (2D) band confirming the formation of RGO. Inset of the Figure 10.9 (b) shows the Raman spectrum of pure $\gamma\text{-Fe}_2\text{O}_3$ which reveals all the characteristic bands of $\gamma\text{-Fe}_2\text{O}_3$ in the low frequency

region, i.e., Eg mode (245, 294, 301, 422, 611), A1g mode (513) confirming the presence of γ -Fe₂O₃. [65] A broad 2D peak due to the presence of RGO has been observed in all three spectra of RGO, RF and RF13 and a slight right shift in the peak position from RGO and RF to RF13 has also been observed. The bands at 1167 and 1623 cm⁻¹, assigned to C–H, and C–C of benzenoid units, respectively, have been observed in PANI spectrum (PRF10) [66]. The same bands have been observed for PANI composites with a slight blue shift, i.e., 1167 to 1172 cm⁻¹ and 1623 to 1625 cm⁻¹. Another band at 1321 cm⁻¹ related to C–N stretching modes of delocalized polaronic charge carriers which is characteristic of the protonated imine form of PANI [67] has also been observed. This band has shifted to 1342 from 1321 cm⁻¹ with the incorporation of RF. Slight shifting in the bands is an evidence of interaction between these components. In addition to this, the low frequency mode of γ -Fe₂O₃ has also been seen in RF and PRF13 samples due to the presence of γ -Fe₂O₃ in the material.

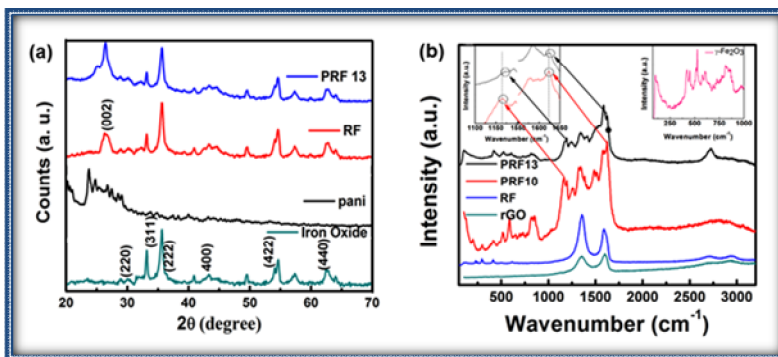


FIGURE 10.9

(a) XRD of γ -Fe₂O₃, pristine PANI, RF and PRF13, (b) Raman spectra of rGO, RF, PRF10, PRF13 and Inset image shows the raman spectra of γ -Fe₂O₃. Reprinted with permission from ref. 15. Copyright 2014, Royal Society of Chemistry

Conductivity, magnetic & dielectric properties of the composites

The room temperature electrical conductivity of composites (Figure 10 a) increases sharply on higher loading of γ -Fe₂O₃ decorated rGO, i.e., from 21.49 Scm⁻¹ (PRF10) to 53.83 Scm⁻¹ (PRF13). This is attributed to two reasons. Firstly, the rGO sheets possess very good conductivity. Secondly, the conducting network is improved on higher wt% loading of RF particles resulting in enhancement of electrical conductivity of the composites. Most importantly, these samples show optimum value of conductivity and magnetization which is desired for exhibiting good microwave shielding responses. [31, 68]

The field dependence of magnetization for the PANI composite containing different wt.% of rGO decorated with γ -Fe₂O₃ nanoparticles have been studied by using the M–H curve at room temperature as shown in Figure 10 (b). The saturation magnetization (M_s) value of the γ -Fe₂O₃ has been found to be 29.15 emug⁻¹ at an external field of 5 kOe having a small value of coercivity and negligible retentivity with no hysteresis loop, indicating a super paramagnetic nature. When these nanoferrite particles are incorporated in the rGO matrix in 1:1 weight ratio, the M_s value has been found to be 16.25 emug⁻¹. Furthermore, it is expected that M_s value may greatly decrease of PANI composites (e.g. in PRF11 M_s value decreases from 16.25 to 2.47 emug⁻¹) because iron oxide is encapsulated in polymer tubes. The role of the tube thickness is important to control the sufficient magnetization value which is required

for EMI shielding applications. We have done several trial to optimize the concentration of polymer in the composite to control the magnetization, efficient capping as well as optimum conductivity for shielding application M_s values of different PANI composites have been measured and given in the Table 1 (see supporting material document). The ferromagnetic properties of composites further confirm that the oxide in the present investigation is γ - Fe_2O_3 rather than Fe_3O_4 which is also supported by the XRD pattern. M_s value of PANI composite increases with the increase of RF loading due to the higher content γ - Fe_2O_3

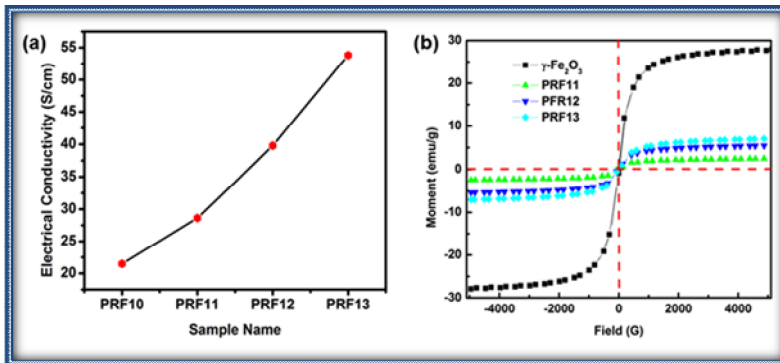


FIGURE 10.10

(a) Variation of electrical conductivity (σ_{dc}) of rGO, iron oxide loaded PANI composites, (b) Vibrating sample magnetometer plots of γ - Fe_2O_3 and PANI composites. Reprinted with permission from ref. 15. Copyright 2014, Royal Society of Chemistry

The EM parameters, i.e., relative complex permittivity ($\epsilon^* = \epsilon' - i\epsilon''$) and relative complex permeability ($\mu^* = \mu' - i\mu''$) have been measured at room temperature for the study of microwave absorption properties of PANI composites which are shown in Figure 10.11 (a-f). These obtained complex parameters have been estimated from experimental scattering parameters (S_{11} & S_{21}) by standard Nicholson-Ross and Weir theoretical calculations [33].

The estimated real part of the EM parameters (ϵ' , μ') is directly associated with the amount of polarization occurring in the material which symbolizes the storage ability of the electric and magnetic energy, while the imaginary part (ϵ'' , μ'') signifies the dissipated electric and magnetic energy.

From Figure 10.11 (a), for PANI composites PRF11, PRF12 and PRF13, the values of ϵ' are in the range of 121.82-84.68, 206.94-130.93, and 339.45-233.77, respectively, which are higher than the pristine PANI (71.94-42.60) in the frequency range 8.2 to 12.4 GHz. Meanwhile, the value of ϵ'' for PRF11, PRF12 and PRF13, are in the range of 77.35-44.27, 129.60-82.58 and 166.28-74.39, respectively, which are also higher than pure PANI (41.78-36.35) as shown in Figure 10.11 (b). It is observed that the samples with higher wt% loading of RF show higher values of ϵ' and ϵ'' due to higher conductivity of RF. It is proposed that more rGO plates may enhance the conductivity and electric polarization because the relative complex permittivity is a measure of the polarizability of a material which induces dipolar and electric polarization in the presence of microwave.

As shown in Figure 10.11 (c) for PANI composites PRF11, PRF12 and PRF13, the values of μ' are in the range of 0.69-0.70, 0.98-1.15 and 1.41-1.71, respectively, which are higher than the pristine PANI (0.16-0.18,) in the X-band. Meanwhile, the value of μ'' for PRF11, PRF12 and PRF13 are in the range of 0.09-0.05, 0.11-0.02 and 0.49-0.50 respectively, which are almost equal to pure PANI (0.08-0.02), as shown in Figure 10.11 (d). Dielectric tangent loss ($\tan \delta_E = \epsilon''/\epsilon'$) and the magnetic tangent loss ($\tan \delta_M = \mu''/\mu'$)

of PANI composites are also calculated using the permittivity and permeability parameters of the samples and presented in Figure 10.11 (e) and (f), respectively. The observed $\tan \delta_{\epsilon}$ is always greater than 0.3 in the entire frequency range indicating that the dielectric loss occurs in all frequency ranges. These results suggest that PANI composites have distinct dielectric loss properties.

According to, the EM theory, dielectric losses are the result of complex phenomena like natural resonance, dipole relaxation, electronic polarization and its relaxation, polarization of polarons and bipolarons in the polymer matrix and their relaxation and certainly the unique structure of the shield. Iron oxide nanoparticles decorated rGO sheet, due to its high conductivity, act as a polarized centre inside the PANI tube which results in more microwave absorption. High aspect ratio of the PANI tubes filled with RF nanoparticles having high conductivity also enhances the absorption properties. In PANI composites, the existence of interfaces between iron oxide nanoparticles and rGO layer, iron oxide and PANI as well as between rGO and PANI. Ferromagnetic nanoparticles act as tiny dipoles which get polarized in the presence of EM field and result in better microwave absorption.

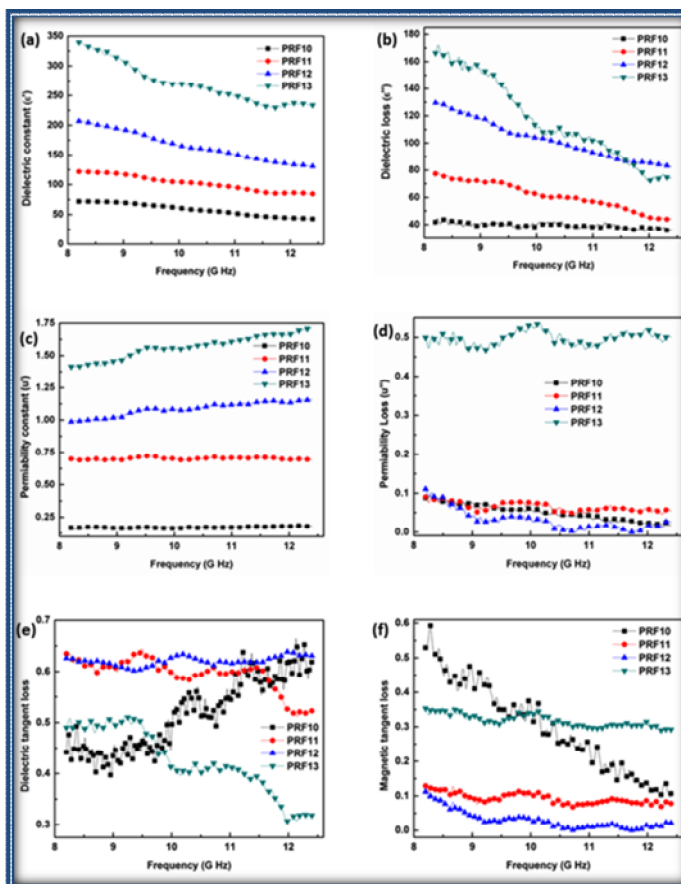


FIGURE 10.11

Frequency dependence of the (a) real parts and (b) imaginary parts of the complex permittivity, (c) real parts and (d) imaginary parts of permeability and the corresponding (e) dielectric loss tangents and (f) magnetic loss tangents of PANI composites. Reprinted with permission from ref. 15. Copyright 2014, Royal Society of Chemistry

PANI and RF nanoparticles and between PANI-PANI tubes, are responsible for interfacial polarization which further contribute to dielectric losses. Interfacial polarization occurs in heterogeneous media due to accumulation of charges at the interfaces and the formation of large dipoles. Figure 10.11 (b) shows that ϵ'' increases with the higher wt.% loading of RF, this is attributed to a conducting network formed by nano ferrite particles decorated rGO sheets. In addition, the conductivity of the samples is further improved by conducting PANI tubes and results in the increase of dielectric loss. Moreover, the dielectric loss is also improved by polaron and bipolaron hopping in PANI matrix which has been reported earlier.[69] The magnetic loss ($\tan \delta_M$) is a result of eddy current effects, natural resonances and anisotropy energy present in the composites. In the microwave ranges, the presence of nano ferrite particles in the composite are the main cause of eddy current. The natural resonances in the X-band can be attributed to the small size of $\gamma\text{-Fe}_2\text{O}_3$ on the rGO sheet. Anisotropy energy of the small size materials,[70] especially in the nanoscale, would be higher due to surface anisotropic field due to the small size effect.[71] The higher anisotropy energy also contributes in the enhancement of the microwave absorption.

Electromagnetic shielding

EMI SE of any material can be expressed as[5, 11, 20, 31, 69, 72]

$$SE(dB) = SE_R + SE_A + SE_M = 10 \log(P_T / P_I) = 20 \log(E_T / E_I) \quad (1)$$

where, P_I (E_I) and P_T (E_T) are the power (electric field intensity) of incident and transmitted EM waves, respectively. The terms in equation 1 can be defined as

$$SE_R = -10 \log(1 - R) \quad (2)$$

$$SE_A = -10 \log(1 - A_{eff}) = -10 \log(T / 1 - R) \quad (3)$$

SE_R , SE_A and SE_M represents shielding effectiveness due to reflection, absorption and multiple reflections respectively, The correction term SE_M can be ignored in all practical application when $SE > 10$ dB [73, 74].

In two port measurement, S- parameters S_{11} (S_{22}), S_{12} (S_{21}) represents the reflection and transmission coefficients given as $T = |S_{21}|^2 = |S_{12}|^2$ and $R = |S_{11}|^2 = |S_{22}|^2$ while the absorption coefficient (A) is defined as $A = 1 - R - T$. Therefore, the effective absorbance (A_{eff}) can be described as $A_{eff} = (1 - R - T) / (1 - R)$ with respect to the power of the effectively incident EM wave inside the shielding material. Figure 10.12 shows the variation of these coefficients as a function of frequency.

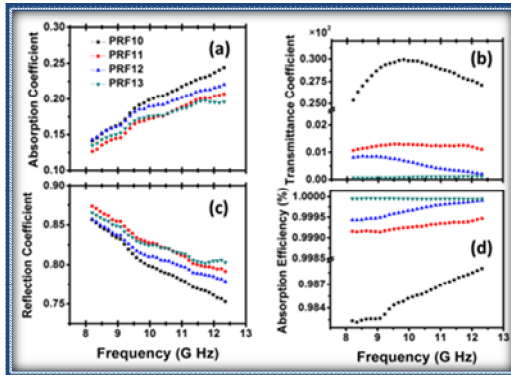


FIGURE 10.12

Absorption coefficient (a), reflection coefficient (b), Transmission coefficient (c) and absorption efficiency (d) of the as synthesized PANI composites

For a material, the skin depth (δ) is the distance up to which the intensity of the EM wave decreases to $1/e$ of its original strength. The δ is related to angular frequency, relative permeability and total conductivity $\sigma_T = (\sigma_{dc} + \sigma_{ac})$. According to EM theory, for electrically thick samples ($t > \delta$), frequency (δ) dependence of far field losses can be expressed in the terms of total conductivity (σ_T real permeability (μ'), skin depth (δ) and thickness (t) of the shield material as: [74]

$$SE_R(dB) = 10 \log \{ \sigma_{ac} / 16\omega\epsilon_0\mu' \} \quad (4)$$

$$SE_A(dB) = 20 \{ t / \delta \} \log e = 20d \sqrt{\mu\omega\sigma_{ac}} / 2 \log e = 8.68 \{ t / \delta \} \quad (5)$$

The σ_{ac} and δ can be related to the imaginary permittivity (ϵ'') and real permeability (μ') as $\sigma_{ac} = \omega\epsilon_0\epsilon''$ and $\delta = \sqrt{2 / \sigma\omega\mu'}$, which gives absorption loss as:

$$SE_A(dB) = 8.68t \sqrt{\sigma\omega\mu' / 2} \quad (6)$$

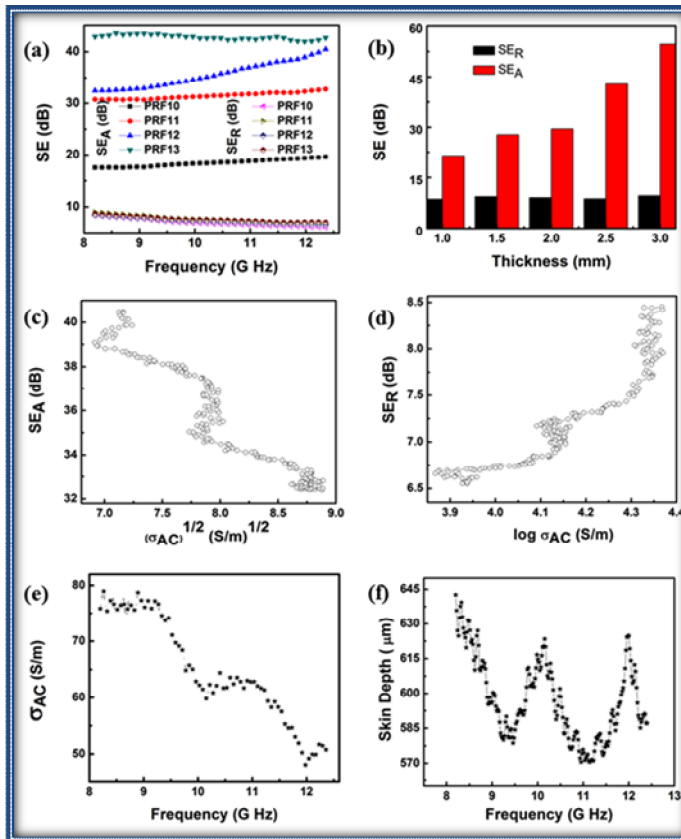


FIGURE 10.13

(a) EMI SE of PANI composites having different wt.% ratio of RF, (b) SE of PRF13 composite with different thickness, (c) dependence of SE_A as a function of $(\sigma_{ac})^{1/2}$ while (d) variation of SE_R as a function of $\log \sigma_{ac}$, (e) shows the variation of σ_{ac} with the increase in frequency and (f) shows change in skin depth with increase in frequency for the sample PRF13. Reprinted with permission from ref. 15. Copyright 2014, Royal Society of Chemistry

SE_A becomes more dominant as compared to the SE_R in the microwave range. This may be caused by the shallow skin depth and high conductivity (σ_{ac}) values at such high frequencies [73, 74] Figure 10.13 (a) shows the variation of the SE with frequency in the 8.2–12.4 GHz range. From the experimental measurement, the SE due to absorption (SE_A) of PANI composites has been found to vary from 17 to 43 dB with increase in the γ - Fe_2O_3 content while the SE_R remains nearly constant at 9 dB. Thus, the total SE achieved for the composite is 51 dB (PRF13) which is higher than the pristine PANI (PRF10). It has been observed that for conducting PANI composite, SE is mainly dominated by absorption while the SE_R is constant. It is observed that the thickness of the shield has a great influence on the microwave absorbing properties as shown in Figure 10.13 (b). Our PANI composites exhibit better microwave absorbing properties in comparison with pristine PANI, [63] pure rGO, γ - Fe_2O_3 nanoparticles, [75] PANI- γ - Fe_2O_3 composite, [75] PANI/multiwall carbon nanotubes composite, [76, 77] PANI rGO iron oxide composites [78] reported earlier.

To relate σ_{ac} with the shielding parameter of the material, SE_A has been plotted against $(\sigma_{ac})^{1/2}$, (Figure 10.13 (c)). The skin depth of the samples has been calculated using the relation, $\delta = \sqrt{2/\omega\mu\sigma_{ac}}$ and its

variation with frequency has been shown in Figure 10.13 (f). It can be noticed that the skin depth is constant in the overall frequency range which demonstrates the surface conduction as shown in figure exists in the whole frequency range. The Skin depth of PANI composite is very small ($600 \mu\text{m}$), due to the high electrical conductivity and good magnetic properties. From equation 6, it is seen that better SE_A can be achieved from moderate conducting materials.

The dependence of SE_R as a function of $\log \sigma_{ac}$ is shown in Figure 10.13 (d) while Figure 10.13 (e) shows the variation of σ_{ac} with the increase in frequency for the sample PRF13 calculated from the dielectric measurements ($\sigma_{ac} = \omega \epsilon_0 \epsilon''$). Therefore, moderate value of conductivity (σ_{ac}) is required for materials having less SE due to reflection.

The excellent microwave absorbing performance of PANI composites is mainly attributed to two factors: impedance matching and EM wave attenuation. The ideal condition for the perfect absorber is $\epsilon_r = \mu_r$, the presence of rGO sheet decorated with insulating magnetic $\gamma\text{-Fe}_2\text{O}_3$ nanoparticles in the core of PANI matrix has lowered ϵ_r of the composite, and improved the equality of ϵ_r and μ_r , which helps the level of impedance matching.[79] Also, PANI composites have strong microwave absorption due to their dielectric and magnetic loss. Furthermore high aspect ratio of PANI tubes, the existence of residual defects in $\gamma\text{-Fe}_2\text{O}_3$ nanoparticles decorated rGO sheet[80] and multiple reflections within the shield enhances the microwave absorption ability of the composites. To further give a visual demonstration of the microwave absorption mechanism as discussed above a schematic is given in Figure 10.14. From all the above, the results of PANI composites illustrates that these composites could be used as microwave absorbing material.

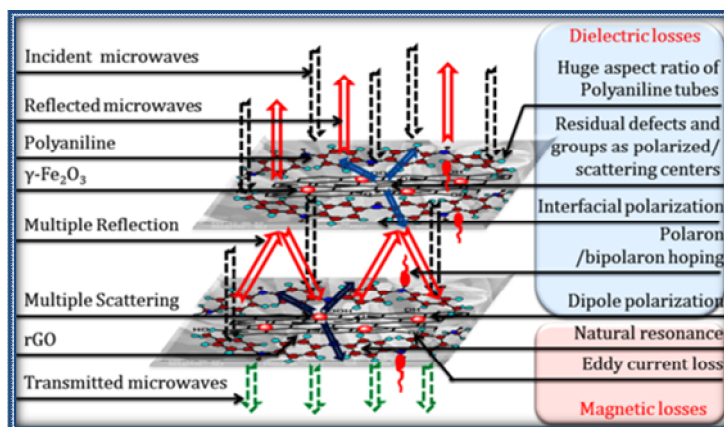


FIGURE 10.14

Schematic presentation of possible microwave absorbing mechanisms in the PANI composites. Reprinted with permission from ref. 15. Copyright 2014, Royal Society of Chemistry

Synthesis of Multiphase Nanocomposites-2 (Synthesis of hybrid composite having $\gamma\text{-Fe}_2\text{O}_3$ nanoparticles, fly ash, and conducting matrix)

Prior to designing hybrid composite, expanded graphite (EG) and reduced graphene oxide (RGO) were synthesized. EG were obtained by mixing natural graphite with mixture of acids consisting of

concentrated H_2SO_4 and HNO_3 by stirring at room temperature and keeping for 24 hours to form the GIC which is then rapidly expanded at temperatures between 800 and 900°C to form EG [81, 82].

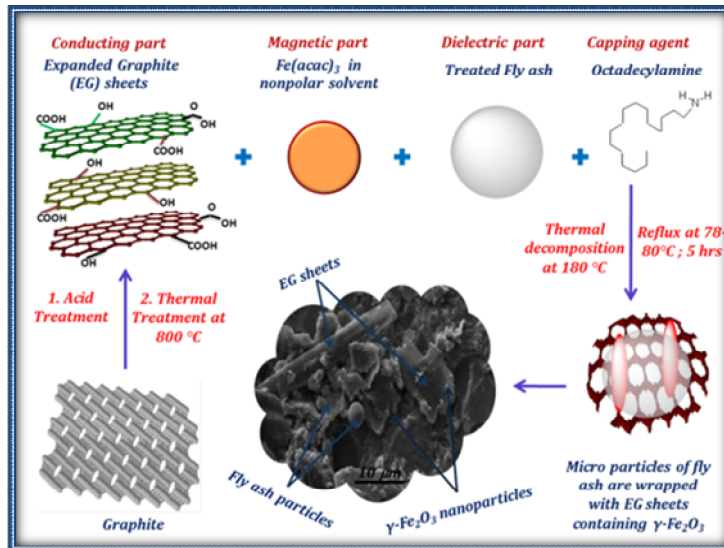


FIGURE 10.15

Schematic representation of preparation of different composites of EG/ $\gamma\text{-Fe}_2\text{O}_3$ /fly ash with varying ratios of EG, $\gamma\text{-Fe}_2\text{O}_3$ and fly ash using ODA as a capping agent in the organic medium. Reprinted with permission from ref. 38. Copyright 2014, Elsevier

RGO were obtained by reducing graphene oxide (GO) using hydrazine hydrate while GO were synthesised using Modified Hummer's process [83, 84] in which graphite powder (5 g) and NaNO_3 (5 g) is mixed into concentrated H_2SO_4 (230 ml). KMnO_4 (40 g) is added gradually with stirring and cooling, so that the temperature of the mixture is not allowed to reach beyond 20 °C. The mixture is then stirred at 35 °C for 2 h, and deionized water (200 ml) is added. The reaction is stirred for 1 hour by the addition of a large amount of deionized water (300 ml) and 30% H_2O_2 solution (30 ml), causing violent effervescence and an increase in temperature to 100°C, after which the color of the suspension changes to bright yellow. The suspension is washed with 1:10 HCl solution (100 ml) in order to remove metal ions. The paste collected is dried at 60 °C. The resultant powder is dispersed in distilled water followed by stirring and ultra-sonication for 3 hours.

The EG, iron acetylacetonate, fly ash and ODA were mixed in methanol and refluxed for 5 hours at 80°C. The subsequent mixture is further heated to 230°C and checked simultaneously with external magnet until the magnetic property appear in the sample. The composites of EG, $\gamma\text{-Fe}_2\text{O}_3$ and fly ash have been formed with varying ratios of EG, $\gamma\text{-Fe}_2\text{O}_3$ and fly ash and are abbreviated as EGFFA111 where EG, $\text{Fe}(\text{acac})_3$ and fly ash are taken in 1:1:1 wt. ratio, EGFFA112 where EG, $\text{Fe}(\text{acac})_3$ and fly ash are taken in 1:1:2 wt. ratio, EGFFA121 for 1:2:1 ratio, EGFFA211 where EG, $\text{Fe}(\text{acac})_3$ and fly ash are taken in 2:1:1 ratio respectively. RGOFFA111 consists RGO, $\text{Fe}(\text{acac})_3$ and fly ash in 1:1:1 ratio. Schematic representation of incorporation of $\gamma\text{-Fe}_2\text{O}_3$ and fly ash into EG matrix is shown in Figure 10.15.

Characterization

Surface morphology and microstructural studies of composite

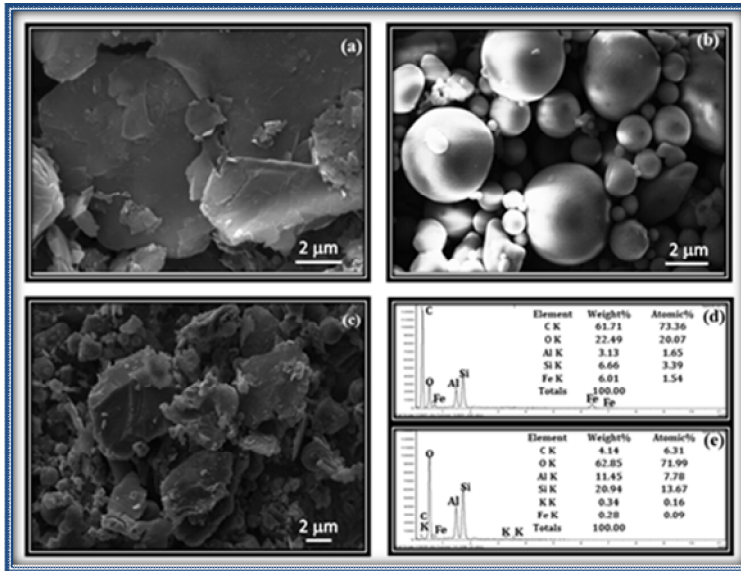


FIGURE 10.16

(a) SEM images of EG sheets, (b) fly ash micro-particles, (c) EGFFA111 having EG, $\text{Fe}(\text{acac})_3$ and fly ash are taken in 1:1:1 wt.% ratio by using ODA as a capping agent in the organic medium, (d) EDS pattern of EGFFA111 composite and (e) EDS pattern of fly ash. Reprinted with permission from ref. 38. Copyright 2014, Elsevier

Scanning electron microscopy (SEM) examination was carried out to determine the distribution of EG, $\gamma\text{-Fe}_2\text{O}_3$ and fly ash in the composites. Figure 10.16 (a) shows the sheets of EG having area of $2\text{-}10\ \mu\text{m}^2$. Determination of thickness of EG platelets is considered difficult by SEM. It is well known that the back scattered electrons (BSE) image provides information on the composition of the sample [85]. The fly ash particle size is seen up to few micrometers as seen in Figure 10.16 (b). Figure 10.16(c) demonstrates that EG sheets containing magnetic nanoparticles are incorporated on fly ash surface and there is some spacing between them. The elemental analysis of the composite has been performed using energy dispersive x-ray spectroscopy (EDS) pattern. Fig 10.16(e) shows the approximate percentage of the constituents of fly ash like SiO_2 , Al_2O_3 , Fe_2O_3 , CaO which is also present in the composite EGFFA111. Figure 10.16(d) shows that the peak of carbon is more intense in the composite.

Figure 10.17 demonstrates the transmission electron microscopy (TEM) images of EG/ $\gamma\text{-Fe}_2\text{O}_3$ /fly ash hybrid structure. Figure 10.17 (a) clearly indicates that fly ash particle ($0.87\ \mu\text{m}$) is covered by sheets of EG containing the $\gamma\text{-Fe}_2\text{O}_3$ particles (15-25 nm). The dispersion of $\gamma\text{-Fe}_2\text{O}_3$ in EG matrix is confirmed by the TEM image Figure 10.17(b). Electron diffraction (Figure 10.17 (c)) pattern of the EGFFA111 show the presence of crystalline ferrite phase in the EG/ $\gamma\text{-Fe}_2\text{O}_3$ /fly ash composites. The presence of conducting, magnetic and dielectric nanoparticles is helpful for the proper impedance matching, which is necessary for enhancing the absorption of the electromagnetic wave.

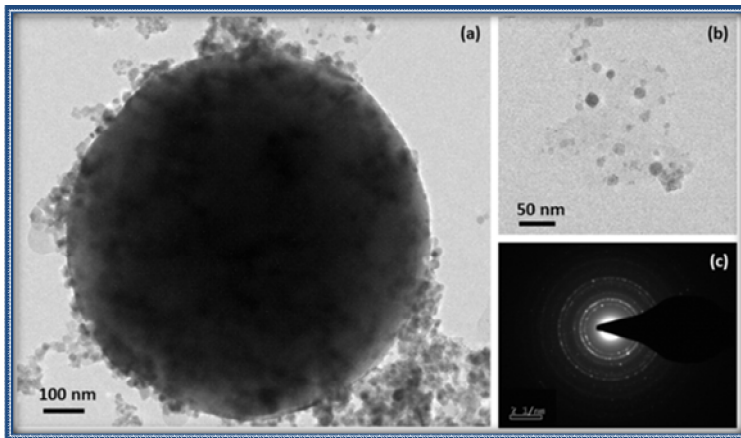


FIGURE 10.17

(a) Transmission electron micrograph image of EG/ γ -Fe₂O₃/fly ash (EGFFA111), (b) EG/ γ -Fe₂O₃ hybrid structure, showing the nanoparticles of γ -Fe₂O₃ on the surface of EG single layer and (c) Electron diffraction pattern of composite EGFFA111. Reprinted with permission from ref. 38. Copyright 2014, Elsevier

Structural Analysis

Figure 10.18 shows the XRD spectra of fly ash, expanded graphite, γ -Fe₂O₃ and EG/ γ -Fe₂O₃/fly ash composite having wt% ratio 1:1:1. The main peaks of expanded graphite are observed at $2\theta=26.524^\circ$ ($d=3.347 \text{ \AA}$) and $2\theta=54.821^\circ$ ($d=1.673 \text{ \AA}$). The main peaks for γ -Fe₂O₃ are observed at $2\theta=30.263^\circ$ ($d=2.9530 \text{ \AA}$), $2\theta=35.659^\circ$ ($d=2.5177 \text{ \AA}$), $2\theta=49.779^\circ$ ($d=1.83027 \text{ \AA}$), $2\theta=57.321^\circ$ ($d=1.6073 \text{ \AA}$) and $2\theta=62.981^\circ$ ($d=1.4758 \text{ \AA}$) corresponding to the (2 2 0), (3 1 1), (4 0 0), (5 1 1) and (4 4 0) reflections which matches with the standard XRD pattern of γ -Fe₂O₃ (Powder Diffraction File, JCPDS No. 39–1346). The main peaks of fly ash are fixed at $2\theta=26.660^\circ$ ($d=3.3409 \text{ \AA}$), 33.240° ($d=2.6931 \text{ \AA}$), 35.260° ($d=2.5433 \text{ \AA}$), 40.880° ($d=2.2057 \text{ \AA}$), 42.620° ($d=2.1196 \text{ \AA}$), 54.040° ($d=1.6955 \text{ \AA}$), 60.680° ($d=1.5249 \text{ \AA}$) and 64.500° ($d=1.4435 \text{ \AA}$). The peaks present in γ -Fe₂O₃ and fly ash were also observed in EGFFA111 which indicate the presence of ferrite particles and fly ash in the EG matrix. While the presence of EG is confirmed by the broad peaks at $2\theta=26.441^\circ$ ($d=3.368$), $2\theta=54.599^\circ$ ($d=1.679 \text{ \AA}$) in the composite. The average size of γ -Fe₂O₃ particles was calculated using above equation and estimated as 22.91 nm for pure γ -Fe₂O₃ and 20.78 nm for γ -Fe₂O₃ incorporated in composite.

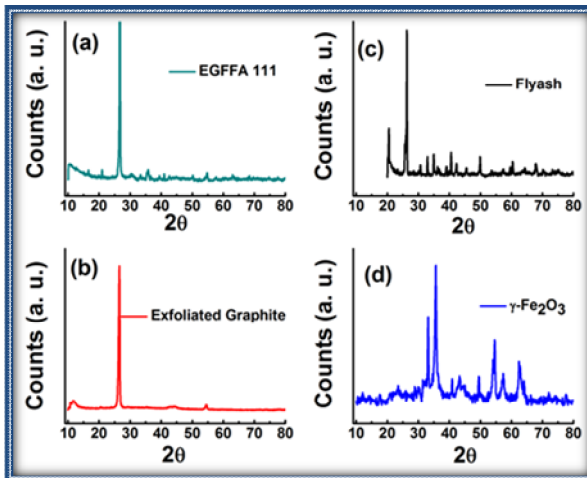


FIGURE 10.18

X-ray diffraction patterns of (a) EGFFA111 having 1:1:1 of EG, γ -Fe₂O₃ and fly ash respectively (b) expanded graphite (c) fly ash, (d) γ -Fe₂O₃. Reprinted with permission from ref. 38. Copyright 2014, Elsevier

Conductivity Measurements

The maximum value of conductivity of the order of 32.86 S/cm is observed for EGFFA211 where EG, Fe(acac)₃ and fly ash are taken in 2:1:1 ratio and minimum value of 0.34 S/cm is observed for EGFFA112 where EG, Fe(acac)₃ and fly ash are taken in 1:1:2 ratio. It is acceptable because the higher wt% of insulating γ -Fe₂O₃ and fly ash particles hinders the free flow of electrons in the composite. According to percolation theory, the electrical conductivity of a material is determined by the ability to form a conducting network. EGFFA211 shows high conductivity because of high wt% loading of EG which forms conducting network. Although electrical conductivity of EG and EGFFA211 is high, but it is much smaller than that of graphene reported theoretically. This is because the inter transport of charge carriers in EG and EGFFA211 is a complex phenomenon of electron tunneling and hopping and is different from single layer of graphene. Due to loading of γ -Fe₂O₃ and fly ash, the electrical conductivity and EMI shielding properties have been adversely affected for composites due to insulating character of fly ash. So the amount of γ -Fe₂O₃ and fly ash has been restricted to 25 wt%.

The electrical conductivity of multiphase composite falls sharply on higher loading of γ -Fe₂O₃ and fly ash. This is contributed to two reasons. Firstly, the γ -Fe₂O₃ and fly ash particles are insulating in nature. Secondly, as we kept the % of γ -Fe₂O₃ fixed and on increasing the loading of fly ash results in reduction in conductivity of EG composites.

Magnetic properties

The magnetic properties of the EG/ γ -Fe₂O₃/fly ash composites have been explained by using the M–H curve (Figure 10.19 (a)). The saturation magnetization (M_s) value of the composite has been found to 2.70 to 6.59 emug⁻¹ at an external field of 5 kOe having small value of coercivity and negligible retentivity with no hysteresis loop, indicating the super paramagnetic nature. When these nanoferrite particles are incorporated in the EG matrix with fly ash in different weight ratio (e.g. 1:1:1 EGFFA111), the magnetization saturation (M_s) value has been found 4.27 emug⁻¹. However, on changing the weight composition of EG/ γ -Fe₂O₃/fly ash to 1:2:1, the M_s value has been increased from 4.27 to 6.59

emu g^{-1} , keeping the external applied field at 5 kOe. M_s value of different EG/ $\gamma\text{-Fe}_2\text{O}_3$ /fly ash composites has been measured. In all the cases very small coercivity is observed with negligible retentivity which indicates the ferromagnetic nature. M_s value increases due to high poly-dispersivity of the $\gamma\text{-Fe}_2\text{O}_3$ in EG matrix with fly ash that arises due to the functionalization of nanoferrite particles with the solution of methanol in presence of EG.

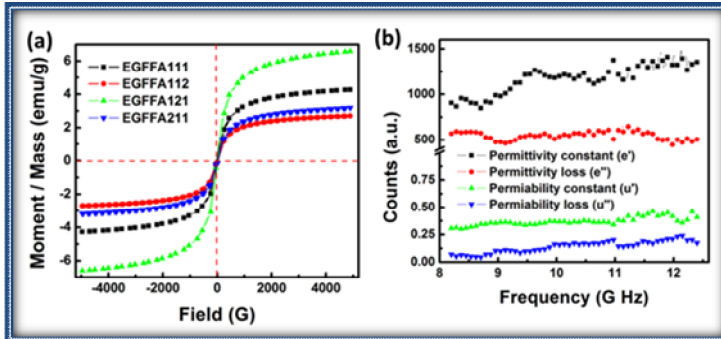


FIGURE 10.19

Vibrating sample magnetometer plots of EG/ $\gamma\text{-Fe}_2\text{O}_3$ /fly ash composites having different weight fraction ratio 1:1:1, 1:1:2, 1:2:1 and 2:1:1. Reprinted with permission from ref. 38. Copyright 2014, Elsevier

Figure 10.20(a) shows the dependence of the EMI SE due to absorption with frequency in the 8.2–12.4 GHz range. From the experimental measurement, the shielding effectiveness due to absorption (SE_A) has been found to vary from 48.76–69.06 dB in the composite EGFFA111 while the SE_R varies from 13.63 to 12.43 dB for the same (See Figure 10.20(b&c)). Thus, the total SE achieved for the fly ash composite is 81.49dB (EGFFA111) which is much higher than the pristine fly ash. It has been observed that for conducting EG/ $\gamma\text{-Fe}_2\text{O}_3$ /fly ash composite, shielding effectiveness (SE) is mainly dominated by absorption while the shielding effectiveness due to reflection (SE_R) is constant and contributes comparatively little. The complex parameters i.e. permittivity ($\epsilon^* = \epsilon' - i\epsilon''$) and permeability ($\mu^* = \mu' - i\mu''$) of EG/ $\gamma\text{-Fe}_2\text{O}_3$ /fly ash composite support in investigating the reasons behind the observed increase in SE. The real part or dielectric constant (ϵ') is mainly associated with the amount of polarization occurring in the material and the imaginary part (ϵ'') is a measure of dissipated energy. The dielectric performance of the material depends on ionic, electronic, orientational and space charge polarization. The contribution to the space charge polarization appears due to the heterogeneity of the material. The presence of insulating magnetic $\gamma\text{-Fe}_2\text{O}_3$ and dielectric fly ash in the conducting matrix results in the formation of more interfaces and a heterogeneous system due to some space charge accumulating at the interface that contributes toward the higher microwave absorption in the composites. The contribution to the orientational polarization is due to the presence of bound charge (magnetic dipoles). When the frequency of the applied field is increased, the dipoles present in the system cannot reorient themselves fast enough to respond to applied electric field, and as a result, dielectric constant decreases. Due to the difference in the dielectric constant and conductivity of $\gamma\text{-Fe}_2\text{O}_3$, fly ash and EG, some charge carriers present in EG have been trapped, and as a result, space charge is developed on the surface of the $\gamma\text{-Fe}_2\text{O}_3$ and fly ash particles and the EG layer. This also leads to the generation of some space charge at the heterogeneous interface leading to field distortion. The contribution of ionic conduction toward the total loss becomes outstanding with decrease in frequency of applied field. With the increase in frequency, the tendency of interfacial polarization is expected to be increased resulting in increase in polarizability. Therefore, with the increase in frequency, ϵ' increases. Figure

10.19(b) shows the dielectric loss (ϵ'') of EGFFA211 composite is due to the EG phase, interfacial polarization between EG, $\gamma\text{-Fe}_2\text{O}_3$ and fly ash phase. Further, the dielectric losses by $\gamma\text{-Fe}_2\text{O}_3$, fly ash and multiple scattering play a crucial role in the enhancement of microwave absorption. This not only enhances the amount of electromagnetic radiation penetrating inside the shield but also increases the effective absorption capability.

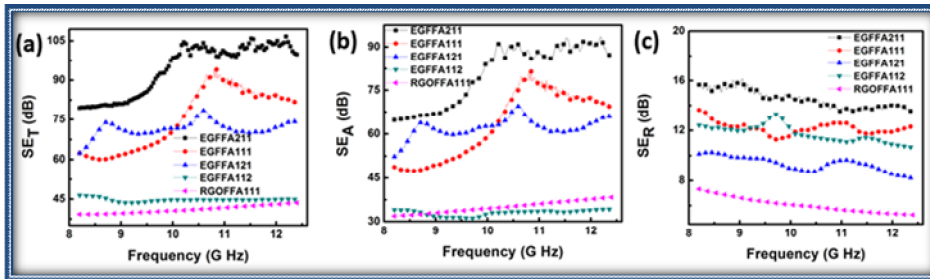


FIGURE 10.20

(a) Variation in EMI shielding effectiveness SE_A of EGFFA111, EGFFA112, EGFFA121, EGFFA211 and RGOFFA111 (b) Behavior of SE_R of different composites (c) shows the total SE as a function of frequency (d) Behavior of permittivity, permittivity loss, permeability and permeability loss of EG/ $\gamma\text{-Fe}_2\text{O}_3$ /fly ash composite having wt. fraction ratio 2:1:1 as a function of frequency. Reprinted with permission from ref. 38. Copyright 2014, Elsevier

Conclusions

The enhanced microwave shielding of multiphase nanocomposite can be achieved either by incorporating the optimum amount of dielectric and magnetic filler in polymer matrix or by designing a matrix that have a mixture of conducting, dielectric and magnetic materials. Although a lot of work has been done in this direction, but the search of a shield that will give complete absorption with no reflection remained a challenged issue. Metamaterials could be act as the next generation microwave shield and seem to be possible solution. Therefore these new light weight multiphase composites with outstanding shielding properties pushes its promising applications in next generation building block material for EMI shielding and stealth technology.

References

1. Hemming LH. Architectural Electromagnetic Shielding Handbook: A Design and Specification Guide: Wiley; 2000.
2. Hanada E, Antoku Y, Tani S, Kimura M, Hasegawa A, Urano S, et al. Electromagnetic interference on medical equipment by low-power mobile telecommunication systems. *Electromagnetic Compatibility, IEEE Transactions on*. 2000;42(4):470-6.
3. Festa A, Panella M, Lo Sterzo E, Roberto, Liparulo L. Radiofrequency Identification Systems for Healthcare: A Case Study on Electromagnetic Exposures. *Journal of Clinical Engineering*. 2013;38(3):125-33

4. Wilson PF, Ma MT, Adams JW. Techniques for measuring the electromagnetic shielding effectiveness of materials. I. Far-field source simulation. *Electromagnetic Compatibility, IEEE Transactions on*. 1988;30(3):239-50.
5. Ohlan A, Singh K, Chandra A, Dhawan SK. Conducting ferromagnetic copolymer of aniline and 3,4-ethylenedioxythiophene containing nanocrystalline barium ferrite particles. *Journal of Applied Polymer Science*. 2008;108(4):2218-25.
6. Zhang H-B, Yan Q, Zheng W-G, He Z, Yu Z-Z. Tough Graphene–Polymer Microcellular Foams for Electromagnetic Interference Shielding. *ACS Applied Materials & Interfaces*. 2011;3(3):918-24.
7. Nalwa HS. *Handbook of Organic Conductive Molecules and Polymers: Conductive polymers: spectroscopy and physical properties*: Wiley; 1997.
8. Al-Saleh MH, U.Sundararaj. Electromagnetic interference shielding mechanism of CNT/polymer composites. *Carbon*. 2009;47 1738-46.
9. Che RC, Peng LM, Duan XF, Chen Q, Liang XL. Microwave Absorption Enhancement and Complex Permittivity and Permeability of Fe Encapsulated within Carbon Nanotubes. *Advanced Materials*. 2004;16(5):401-5.
10. Singh AP, Gupta BK, Mishra M, Govind, Chandra A, Mathur RB, et al. Multiwalled carbon nanotube/cement composites with exceptional electromagnetic interference shielding properties. *Carbon*. 2013;56:86–96.
11. Singh K, Ohlan A, Saini P, Dhawan SK. Poly (3,4-ethylenedioxythiophene) γ -Fe₂O₃ polymer composite–super paramagnetic behavior and variable range hopping 1D conduction mechanism–synthesis and characterization. *Polymers for Advanced Technologies*. 2008;19(3):229-36.
12. Duan Y, Liu S, Guan H. Investigation of electrical conductivity and electromagnetic shielding effectiveness of polyaniline composite. *Science and Technology of Advanced Materials*. 2005;6(5):513.
13. Weir WB. Automatic measurement of complex dielectric constant and permeability at microwave frequencies. *Proc IEEE*. 1974;62:33–6.
14. Wang C, Han X, Xu P, Zhang X, Du Y, Hu S, et al. The electromagnetic property of chemically reduced graphene oxide and its application as microwave absorbing material. *Applied Physics Letters*. 2011;98(7):072906-3.
15. Singh AP, Mishra M, Sambyal P, Gupta BK, Singh BP, Chandra A, et al. Incapsulation of [gamma]-Fe₂O₃ decorated reduced graphene oxide in polyaniline core-shell tubes as an exceptional tracker for electromagnetic environmental pollution. *Journal of Materials Chemistry A*. 2013.
16. Sambyal P, Singh AP, Verma M, Farukh M, Singh BP, Dhawan SK. Tailored polyaniline/barium strontium titanate/expanded graphite multiphase composite for efficient radar absorption. *RSC Advances*. 2014.
17. Gupta TK, Singh BP, Singh VN, Teotia S, Singh AP, Elizabeth I, et al. MnO₂ decorated graphene nanoribbons with superior permittivity and excellent microwave shielding properties. *Journal of Materials Chemistry A*. 2013;2:4256-63.
18. Chen S, Zhu J, Wu X, Han Q, Wang X. Graphene Oxide–MnO₂ Nanocomposites for Supercapacitors. *ACS Nano*. 2010;4(5):2822-30.
19. Liu J, Fu S, Yuan B, Li Y, Deng Z. Toward a Universal “Adhesive Nanosheet” for the Assembly of Multiple Nanoparticles Based on a Protein-Induced Reduction/Decoration of Graphene Oxide. *Journal of the American Chemical Society*. 2010;132(21):7279-81.
20. Singh AP, Mishra M, Chandra A, Dhawan SK. Graphene oxide/ferrofluid/cement composites for electromagnetic interference shielding application. *Nanotechnology*. 2011;22:9.

21. Reddy B. *Advances in Nanocomposites - Synthesis, Characterization and Industrial Applications*: InTech; 2011.
22. Bjorklof D. *Shielding for EMC. Shielding for EMC Compliance Engineering*. 1999.
23. Bridges JE. *IEEE Trans EMC*. 1988;30:289.
24. Duffin WJ. *Advanced Electricity and Magnetism* London: McGraw-Hill. 1968.
25. <http://www.ece.msstate.edu/~donohoe/ece4323shielding.pdf>.
26. Paul CR. *Electromagnetics for Engineers*, Wiley, Hoboken, NJ. 2004.
27. Ott HW. *Noise Reduction Techniques in Electronic Systems*, 2nd ed New York: John Wiley & Sons. 1988.
28. Schulz RB, Plantz VC, Brush DR. *Shielding theory and practice*, *IEEE Trans Electromagn Compat EMC*. 1988;30(187).
29. Schelkunoff SA. *Electromagnetic Waves*, Van Nostrand, NJ. 1943.
30. Ashokkumar M, Narayanan NT, Gupta BK, Reddy ALM, Singh AP, Dhawan SK, et al. *Conversion of Industrial Bio-Waste into Useful Nanomaterials*. *ACS Sustainable Chemistry & Engineering*. 2013;1(6):619-26.
31. Singh AP, Garg P, Alam F, Singh K, Mathur RB, Tandon RP, et al. *Phenolic resin-based composite sheets filled with mixtures of reduced graphene oxide, c-Fe₂O₃ and carbon fibers for excellent electromagnetic interference shielding in the X-band*. *Carbon*. 2012;50:3868-75.
32. Tong XC. *Advanced Materials and Design for Electromagnetic Interference Shielding*: CRC Press; 2008.
33. Nicolson AM, Ross GF. *Measurement of the intrinsic properties of materials by time-domain techniques*. *IEEE Trans Instrum Mea*. 1970;19 377-82.
34. *Application Note A, Basics of Measuring the Dielectric Properties of Materials*, <http://www3.imperial.ac.uk/pls/portallive/docs/1/11949698.PDF>.
35. Mishra M, Singh AP, Dhawan SK. *Expanded graphite-nanoferrite-fly ash composites for shielding of electromagnetic pollution*. *Journal of Alloys and Compounds*. 2013;557:244-51.
36. Singh AP, Mishra M, Chandra A, Dhawan SK. *Graphene oxide/ferrofluid/cement composites for electromagnetic interference shielding application*. *Nanotechnology*. 2011;22(46):465701.
37. http://en.wikipedia.org/wiki/Dielectric_spectroscopy.
38. Das CK, Mandal A. *Microwave Absorbing Properties of DBSA-doped Polyaniline/BaTiO₃-Ni_{0.5}Zn_{0.5}Fe₂O₄ Nanocomposites*. 2012;1(1):43-53.
39. Ohlan A, Singh K, Chandra A, Singh V, Dhawan S. *Conjugated polymer nanocomposites: Synthesis, dielectric, and microwave absorption studies*. *Journal of Applied Physics*. 2009;106(4):044305--6.
40. Singh AP, S. AK, Chandra A, Dhawan SK. *Conduction mechanism in Polyaniline-flyash composite material for shielding against electromagnetic radiation in X-band & Ku band*. *AIP ADVANCES*. 2011;1(2):-.
41. Huang X, Chen Z, Tong L, Feng M, Pu Z, Liu X. *Preparation and microwave absorption properties of BaTiO₃@MWCNTs core/shell heterostructure*. *Materials Letters*. 2013;111(0):24-7.
42. Dhawan SK, Singh K, Bakhshi AK, Ohlan A. *Conducting polymer embedded with nanoferrite and titanium dioxide nanoparticles for microwave absorption*. *Synthetic Metals*. 2009;159(21-22):2259-62.
43. Cheng F, Tang W, Li C, Chen J, Liu H, Shen P, et al. *Conducting Poly(aniline) Nanotubes and Nanofibers: Controlled Synthesis and Application in Lithium/Poly(aniline) Rechargeable Batteries*. *Chemistry - A European Journal*. 2006;12(11):3082 - 8.

44. Xiang C, Pan Y, Liu X, Sun X, Shi X, Guo J. Microwave attenuation of multiwalled carbon nanotube-fused silica composites. *Applied Physics Letters*. 2005;87(12):123103-3.
45. Yuan B, Yu L, Sheng L, An K, Zhao X. Comparison of electromagnetic interference shielding properties between single-wall carbon nanotube and graphene sheet/polyaniline composites. *Journal of Physics D: Applied Physics*. 2012;45.
46. Yonglai Y, Mool CG, Kenneth LD. Towards cost-efficient EMI shielding materials using carbon nanostructure-based nanocomposites. *Nanotechnology*. 2007;18(34):345701.
47. Narayanan T, Sunny V, Shaijumon M, Ajayan P, Anantharaman M. Enhanced microwave absorption in nickel-filled multiwall carbon nanotubes in the S band. *Electrochemical and Solid-State Letters*. 2009;12(4):K21-K4.
48. Zhu Y-F, Zhang L, Natsuki T, Fu Y-Q, Ni Q-Q. Facile Synthesis of BaTiO₃ Nanotubes and Their Microwave Absorption Properties. *ACS Applied Materials & Interfaces*. 2012;4(4):2101-6.
49. Wang L, Huang Y, Sun X, Huang H, Liu P, Zong M, et al. Synthesis and microwave absorption enhancement of graphene@Fe₃O₄@SiO₂@NiO nanosheet hierarchical structures. *Nanoscale*. 2014;6(6):3157-64.
50. Ren Y-L, Wu H-Y, Lu M-M, Chen Y-J, Zhu C-L, Gao P, et al. Quaternary nanocomposites consisting of graphene, Fe₃O₄@Fe core@shell, and ZnO nanoparticles: synthesis and excellent electromagnetic absorption properties. *ACS Applied Materials & Interfaces*. 2012;4(12):6436-42.
51. Xu H-L, Bi H, Yang R-B. Enhanced microwave absorption property of bowl-like Fe₃O₄ hollow spheres/reduced graphene oxide composites. *Journal of Applied Physics*. 2012;111(7):-.
52. Li Q, Pang J, Wang B, Tao D, Xu X, Sun L, et al. Preparation, characterization and microwave absorption properties of barium-ferrite-coated fly-ash cenospheres. *Advanced Powder Technology*. 2013;24(1):288-94.
53. Song W-L, Cao M-S, Lu M-M, Bi S, Wang C-Y, Liu J, et al. Flexible graphene/polymer composite films in sandwich structures for effective electromagnetic interference shielding. *Carbon*. 2014;66(0):67-76.
54. Song W-L, Cao M-S, Lu M-M, Liu J, Yuan J, Fan L-Z. Improved dielectric properties and highly efficient and broadened bandwidth electromagnetic attenuation of thickness-decreased carbon nanosheet/wax composites. *Journal of Materials Chemistry C*. 2013;1(9):1846-54.
55. Seo MA, Yim JH, Ahn YH, Rotermund F, Kim DS, Lee S, et al. Terahertz electromagnetic interference shielding using single-walled carbon nanotube flexible films. *Applied Physics Letters*. 2008;93(23):-.
56. Yang Y, Gupta MC, Dudley KL, Lawrence RW. Novel Carbon Nanotube-Polystyrene Foam Composites for Electromagnetic Interference Shielding. *Nano Letters*. 2005;5(11):2131-4.
57. Sun C, Jiang W, Wang Y, Sun D, Liu J, Li P, et al. Magnetic and electromagnetic absorption properties of FeNi alloy nanoparticles supported by reduced graphene oxide. *physica status solidi (RRL) – Rapid Research Letters*. 2014;8(2):141-5.
58. Brigandi PJ, Cogen JM, Pearson RA. Electrically conductive multiphase polymer blend carbon-based composites. *Polymer Engineering & Science*. 2014;54(1):1-16.
59. Li N, Huang Y, Du F, He X, Lin X, Gao H, et al. Electromagnetic Interference (EMI) Shielding of Single-Walled Carbon Nanotube Epoxy Composites. *Nano Letters*. 2006;6(6):1141-5.
60. Kim HM, Kim K, Lee CY, Joo J, Cho SJ, Yoon HS, et al. Electrical conductivity and electromagnetic interference shielding of multiwalled carbon nanotube composites containing Fe catalyst. *Applied Physics Letters*. 2004;84(4):589-91.
61. Xiang C, Pan Y, Liu X, Shi X, Sun X, Guo J. Electrical Properties of Multiwalled Carbon Nanotube Reinforced Fused Silica Composites. *J Nanosci Nanotechnol*. 2006;6:3835-41.

62. Wang J, Zhou H, Zhuang J, Liu Q. Influence of spatial configurations on electromagnetic interference shielding of ordered mesoporous carbon/ordered mesoporous silica/silica composites. *Sci Rep.* 2013;3.
63. Singh AP, S. AK, Amita Chandra, K.Dhawan S. Conduction mechanism in Polyaniline-flyash composite material for shielding against electromagnetic radiation in X-band & Ku band. *AIP ADVANCES.* 2011;1:022147.
64. K.Gupta T, P.Singh B, R.Dhakate S, Singh VN, Mathur RB. Improved Nanoindentation and Microwave Shielding Properties of Modified MWCNT Reinforced Polyurethane Composites. *Journal of Materials Chemistry A.* 2013.
65. Shim S-H, Duffy TS. Raman spectroscopy of Fe₂O₃ to 62 GPa. *American Mineralogist.* 2002;87:318-26.
66. Silva JEPd, Faria DLAd, Torresi SICd, Temperini MLA. Influence of Thermal Treatment on Doped Polyaniline Studied by Resonance Raman Spectroscopy. *Macromolecules.* 2000;33(8):3077-83.
67. Shakoor A, Rizvi TZ, Nawaz A. Raman spectroscopy and AC conductivity of polyaniline montmorillonite (PANI–MMT) Nanocomposites. *J Mater Sci: Mater Electron.* 2011;22:1076-80.
68. Colaneri NF, Shacklette LW. EMI Shielding Measurements of Conductive Polymer Blends. *IEEE Trans Instrum Meas.* 1992;41:291-7.
69. Ohlan A, Singh K, Chandra A, Singh VN, Dhawan SK. Conjugated polymer nanocomposites: Synthesis, dielectric, and microwave absorption studies. *Journal of Applied Physics.* 2009;106:044305-11.
70. Leslie-Pelecky DL, Rieke RD. Magnetic Properties of Nanostructured Materials. *Chem Mater.* 1996;8(8):1770-83.
71. Chen Y-J, Gao P, Wang R-X, Zhu C-L, Wang L-J, Cao M-S, et al. Porous Fe₃O₄/SnO₂ core/shell nanorods: synthesis and electromagnetic properties. *J Phys Chem C.* 2009;113(23):10061–4.
72. Sachdev VK, Patel K, Bhattacharya S, Tandon RP. Electromagnetic interference shielding of graphite/acrylonitrile butadiene styrene composites. *Journal of Applied Polymer Science.* 2011;120(2):1100-5.
73. Das NC, Das D, Khastgir TK, Chakraborty AC. Electromagnetic interference shielding effectiveness of carbon black and carbon fibre filled EVA and NR based composites. *Composites A.* 2000;31:1069-81.
74. Colaneri NF, Shacklette LW. EMI Shielding Measurements of Conductive Polymer Blends. *IEEE Trans Instrum Meas.* 1992;41:29.
75. Singh K, Ohlan A, Kotnala RK, Bakhshi AK, Dhawan SK. Dielectric and magnetic properties of conducting ferromagnetic composite of polyaniline with Fe₂O₃ nanoparticles. *Materials Chemistry and Physics.* 2008;112:651-8.
76. Kim Y-Y, Yun J, Lee Y-S, Kim H-I. Preparation and Characteristics of Conducting Polymer-Coated MWCNTs as Electromagnetic Interference Shielding Materials. *Carbon.* 2011;12(1):48-52.
77. Yun J, Im JS, Kim H-I, Lee Y-S. Effect of oxyfluorination on electromagnetic interference shielding of polyaniline-coated multi-walled carbon nanotubes. *Colloid Polym Sci.* 2011;289:1749-55.
78. Singh K, Ohlan A, Pham VH, R. B, Varshney S, Jang J, et al. Nanostructured graphene/Fe₃O₄ incorporated polyaniline as a high performance shield against electromagnetic pollution. *Nanoscale.* 2013;5:2411-20.
79. Belaabed B, Wojkiewicz JL, Lamouri S, El Kamchi N, Lasri T. Synthesis and characterization of hybrid conducting composites based on polyaniline/magnetite fillers with improved microwave absorption properties. *Journal of Alloys and Compounds.* 2012;527(0):137-44.

80. Sun X, He J, Li G, Tang J, Wang T, Guo Y, et al. Laminated magnetic graphene with enhanced electromagnetic wave absorption properties. *J Mater Chem C*. 2013;1:765-77.
81. Dhakate SR, Borah SSM, Mathur RB, Dhami TL. Expanded graphite based electrically conductive composites as bipolar plate for PEM fuel cell. *Inter J Hydro Energy*. 2008;33:7146-52.
82. Dhakate SR, Chauhan N, Sharma S, Tawale J, b SS, Sahare PD, et al. An approach to produce single and double layer graphene from re-exfoliation of expanded graphite. *Carbon*. 2011;49:1946-054.
83. Laura JC, Franklin K, Huang J. Graphene Oxide Sheets at Interfaces. *J Am Chem Soc*. 2009;131:1043.
84. Tung VC, Allen MJ, Yang Y, Kaner RB. High-throughput solution processing of large-scale graphene. *Nature Nanotechnology*. 2009;4:25 - 9.
85. Fang H, Wu Y, Zhao J, Zhu J. Silver catalysis in the fabrication of silicon nanowire arrays. *Nanotechnology*. 2006;17:3768.